

Gravitational waves from nonspinning black hole-neutron star binaries: dependence on equations of state

Koutarou Kyutoku, Masaru Shibata

Yukawa Institute for Theoretical Physics, Kyoto University, Kyoto 606-8502, Japan

Keisuke Taniguchi

Graduate School of Arts and Sciences, University of Tokyo, Komaba, Meguro, Tokyo 153-8902, Japan

(Dated: October 22, 2018)

We report results of a numerical-relativity simulation for the merger of a black hole-neutron star binary with a variety of equations of state (EOSs) modeled by piecewise polytropes. We focus, in particular, on the dependence of the gravitational waveform at the merger stage on the EOSs. The initial conditions are computed in the moving-puncture framework, assuming that the black hole is nonspinning and the neutron star has an irrotational velocity field. For a small mass ratio of the binaries (e.g., $M_{\text{BH}}/M_{\text{NS}} = 2$, where M_{BH} and M_{NS} are the masses of the black hole and neutron star, respectively), the neutron star is tidally disrupted before it is swallowed by the black hole irrespective of the EOS. Especially for less-compact neutron stars, the tidal disruption occurs at a more distant orbit. The tidal disruption is reflected in a cutoff frequency of the gravitational-wave spectrum, above which the spectrum amplitude exponentially decreases. A clear relation is found between the cutoff frequency of the gravitational-wave spectrum and the compactness of the neutron star. This relation also depends weakly on the stiffness of the EOS in the core region of the neutron star, suggesting that not only the compactness but also the EOS at high density is reflected in gravitational waveforms. The mass of the disk formed after the merger shows a similar correlation with the EOS, whereas the spin of the remnant black hole depends primarily on the mass ratio of the binary, and only weakly on the EOS. Properties of the remnant disks are also analyzed.

PACS numbers: 04.25.D-, 04.30.-w, 04.40.Dg

I. INTRODUCTION

Gravitational-wave observation is becoming one of the reliable tools for observing our Universe. Current ground-based laser-interferometric gravitational-wave detectors such as LIGO [1] and VIRGO [2] have already achieved nontrivial scientific results; e.g., upper limits on the amplitude of a stochastic gravitational-wave background have been improved and we now know that gravitational waves are not the main energy source of our Universe [3]. Advanced gravitational-wave detectors such as advanced LIGO will be in operation within the next several years and detect gravitational waves, which can be used to explore the nature of strongly gravitating phenomena. The most promising sources of gravitational waves are the coalescing compact binaries composed of compact objects such as black holes (BHs) and neutron stars (NSs). As illustrated in this paper, black hole-neutron star (BH-NS) binaries are potential sources for exploring the nature of the NSs and high-density nuclear matter.

According to a statistical study based on population synthesis calculations, the detection rate of gravitational waves from BH-NS binaries is estimated to be 0.5–50 events per year for advanced gravitational-wave detectors [4, 5]. This suggests that we will observe a variety of BH-NS binaries in the next decade. To extract physical information of BH-NS binaries as well as the information about the BH and NS themselves from gravitational waves, theoretical templates of gravitational waves are

necessary. This fact motivates the numerical-relativity community to study in depth the coalescence of BH-NS binaries, because numerical relativity is the unique approach for accurately computing gravitational waves emitted from the late inspiral and merger phases of such compact binaries.

Another astrophysical interest in BH-NS binaries is motivated by their potential to be a progenitor of short-hard gamma-ray bursts (GRBs); see [6, 7] and references therein for reviews. According to a merger scenario of GRBs, a NS is tidally disrupted by a low-mass BH before the orbit reaches an innermost stable circular orbit (hereafter ISCO), resulting in a system consisting of a rotating BH and a hot, massive accretion disk of mass $\gtrsim 0.01M_{\odot}$ which could become the central engine of a GRB. This BH-massive disk system could subsequently radiate a large amount of energy $\gtrsim 10^{48}$ erg by neutrino emission or by the so-called Blandford-Znajek process [8] in a short time scale $\lesssim 1$ s. Then, neutrino-anti neutrino pair annihilation or electromagnetic Poynting flux could drive a GRB. One of the key questions for the merger scenario is whether the tidal disruption could lead to formation of the BH-disk system. Numerical relativity is again the unique approach for answering this question.

The equation of state (EOS) of NSs, which is still unknown, is the key for determining gravitational waveforms emitted in the tidal-disruption phase as well as for determining other properties of the BH-disk system such as the mass and typical density of the disk. The EOS (specifically its stiffness) determines the relation between

mass and radius of a NS, and hence, the relation between the tidal-disruption process and associated gravitational waveforms. The reason is that the sensitivity of a NS to the tidal force by the companion BH depends on its radius; e.g., a NS of larger radius (with a stiffer EOS) will be disrupted at a larger orbital separation (or a lower orbital frequency). If the tidal disruption of a NS occurs at a larger distance, more material may be spread around the companion BH, and consequently, a high-mass remnant disk may be formed. Also, the gravitational-wave frequency at the tidal disruption, which will be one of the characteristic frequencies, is lower for NSs of larger radius. The EOS of nuclear matter beyond the normal nuclear density is highly uncertain due to the lack of constraints obtained from experiments. Gravitational-wave astronomy will become a new and robust tool for determining or at least constraining the EOS at such high densities through the observation of NSs [9–12]. For this purpose, we need theoretical templates of gravitational waves and it is necessary to perform many simulations employing a wide variety of possible EOSs for the NS matter.

In recent years, fully general relativistic studies of BH-NS binaries have been performed both in calculations of quasiequilibrium states [13–17] and in dynamical simulations of the mergers [18–25]. However, we have not yet understood the effect of the EOS on the merger of BH-NS binaries in spite of its importance; in most of the previous studies, NSs are modeled by simple and unrealistic $\Gamma = 2$ polytropic EOS (but see [25]). One of the next goals in numerical relativity is to clarify the effect of the EOS on the merger process of BH-NS binaries and on resulting gravitational waveforms. For this purpose, a systematic parametrization of possible EOSs by a small number of parameters is quite useful.

In this paper, we report new results obtained by a simulation using a wide variety of piecewise polytropic EOSs, which are shown to be useful for parametrizing nuclear-theory-based EOSs in the cold approximation [11, 26, 27] [28]. We employ eight types of the piecewise polytropic EOSs, ranging from highly stiff to soft ones [29]. We systematically choose the BH and NS masses in a realistic range of interest. As a first step in this series of work, the BH is assumed to be nonspinning. We track orbital evolutions of BH-NS binaries typically for ~ 5 orbits so that the orbital eccentricity would not give a serious error in gravitational waveforms at the onset of the merger phase. We clarify the dependence of gravitational waveforms and merger remnants on the EOS. In particular, we show that a gravitational-wave spectrum contains valuable information on the EOS properties.

This paper is organized as follows. In Sec. II A, we summarize initial conditions employed in this paper. Section II B describes the piecewise polytropic EOS and the models adopted in this paper. Section III describes the formulation and methods of numerical simulations. Section IV presents the numerical results and clarifies the effect of the EOS on gravitational waveforms and merger

remnants. Section V is devoted to a summary. Throughout this paper, we adopt the geometrical units in which $G = c = 1$, where G and c are the gravitational constant and the speed of light, respectively. The irreducible mass of the BH, gravitational mass of the NS in isolation, circumferential radius of the NS in isolation, Arnowitt-Deser-Misner (ADM) mass of the system, and sum of the BH and NS masses at infinite separation are denoted by $M_{\text{BH}}, M_{\text{NS}}, R_{\text{NS}}, M, m_0 = M_{\text{BH}} + M_{\text{NS}}$, respectively. The mass ratio Q is defined by $Q \equiv M_{\text{BH}}/M_{\text{NS}}$ and the compactness of the NS (\mathcal{C}) is defined by $\mathcal{C} \equiv M_{\text{NS}}/R_{\text{NS}}$. Latin and Greek indices denote spatial and spacetime components, respectively.

II. INITIAL CONDITION

We employ BH-NS binaries in quasiequilibria for initial conditions of numerical simulations as in [20, 24]. The quasiequilibrium state is computed in the moving-puncture framework [17–19] with a piecewise polytropic EOS [11, 26, 27]. Here, we first summarize the formulation and numerical methods for computing the quasiequilibrium state and then describe EOSs employed in this paper. The details of the formulation and methods for computing initial conditions are described in [17], to which the reader may refer. Computation of the quasiequilibrium state is performed using the spectral-method library LORENE [30].

A. Formulation and methods

We derive quasiequilibrium states of BH-NS binaries as solutions of the initial value problem of general relativity [31]. When the orbital separation of the binary is large enough, the time scale for the gravitational-wave emission, t_{GW} , is much longer than the orbital period P_{orb} , so that we can safely neglect the radiation reaction of the gravitational-wave emission. In numerical simulations, the orbital evolution has to be followed for $\gtrsim 5$ orbits to derive a realistic waveform both for the late inspiral and merger phases. For such a purpose, we have to choose the initial separation of the binary which satisfies $t_{\text{GW}} \gg P_{\text{orb}}$, and have to provide BH-NS binaries in a quasicircular orbit as the initial condition, i.e., the binary is approximately in an equilibrium state if it is observed in the comoving frame. To satisfy these two conditions, we assume the presence of a helical Killing vector field with the orbital angular velocity Ω ,

$$\xi^\mu = (\partial_t)^\mu + \Omega(\partial_\varphi)^\mu, \quad (1)$$

and a hydrostatic equilibrium for the fluid configuration in the comoving frame. In addition, we assume that the BH is nonspinning and the NS has an irrotational velocity field. The irrotational velocity field is believed to be an astrophysically (approximately) realistic configuration [32, 33].

To compute the three-metric γ_{ij} , the extrinsic curvature K_{ij} , the lapse function α , and the shift vector β^i , we employ a mixture of the conformal thin-sandwich approach and the conformal transverse-traceless decomposition of Einstein's equation [31]. We assume the conformal flatness of the three-metric $\gamma_{ij} = \psi^4 \hat{\gamma}_{ij} = \psi^4 f_{ij}$, the stationarity of the conformal three-metric $\partial_t \hat{\gamma}_{ij} = 0$, and the maximal slicing condition for the trace part of the extrinsic curvature $K = \gamma^{ij} K_{ij}$, i.e., $K = \partial_t K = 0$. Here, f_{ij} denotes the flat spatial metric. Then, the basic equations for the conformal factor ψ , the shift vector β^i , and a weighted lapse function $\Phi \equiv \alpha\psi$ are derived from the Hamiltonian constraint, the momentum constraint, and the maximal slicing condition $\partial_t K = 0$ as

$$\Delta\psi = -2\pi\psi^5\rho_H - \frac{1}{8}\psi^{-7}\hat{A}_{ij}\hat{A}^{ij}, \quad (2)$$

$$\Delta\beta^i + \frac{1}{3}\hat{\nabla}^i\hat{\nabla}_j\beta^j = 16\pi\Phi\psi^3j^i + 2\hat{A}^{ij}\hat{\nabla}_j(\Phi\psi^{-7}), \quad (3)$$

$$\Delta\Phi = 2\pi\Phi\psi^4(\rho_H + 2S) + \frac{7}{8}\Phi\psi^{-8}\hat{A}_{ij}\hat{A}^{ij}, \quad (4)$$

where $\hat{A}^{ij} \equiv \psi^{10}K^{ij}$, $\Delta \equiv f^{ij}\hat{\nabla}_i\hat{\nabla}_j$, and $\hat{\nabla}_i$ denotes the covariant derivative associated with f_{ij} . We assume an ideal fluid for the matter field

$$T^{\mu\nu} = \rho hu^\mu u^\nu + P g^{\mu\nu}. \quad (5)$$

where ρ is the rest-mass density, P is the pressure, $h \equiv 1 + \varepsilon + P/\rho$ is the specific enthalpy, ε is the specific internal energy, and u^μ is the four-velocity of the fluid. Then, the fluid quantities seen by the Eulerian observer are denoted by

$$\rho_H = \rho h(\alpha u^t)^2 - P, \quad (6)$$

$$j^i = \rho h \alpha u^t u^\mu \gamma_\mu^i, \quad (7)$$

$$S = \rho h[(\alpha u^t)^2 - 1] + 3P. \quad (8)$$

The EOS fully determines relations among the thermodynamical quantities ρ , ε , P , and h . We describe the EOS adopted in this work in Sec. II B.

In the moving-puncture framework, we set ψ and Φ as

$$\psi = 1 + \frac{M_P}{2r_{\text{BH}}} + \phi, \quad \Phi = 1 - \frac{M_\Phi}{r_{\text{BH}}} + \eta, \quad (9)$$

where M_P and M_Φ are positive constants of mass dimension and $r_{\text{BH}} = |x^i - x_P^i|$ is a coordinate distance from the puncture located at x_P^i . We numerically solve the nonsingular parts ϕ and η using Eqs. (2) and (4) and adjusting the parameter M_P to achieve a desired BH mass. The other parameter, M_Φ , is determined by the virial relation, i.e., the condition in which the ADM mass (M_0) and the Komar mass agree, which holds for the stationary and asymptotically flat spacetime [34, 35],

$$\oint_{r \rightarrow \infty} \partial_i \Phi dS^i = - \oint_{r \rightarrow \infty} \partial_i \psi dS^i = 2\pi M_0. \quad (10)$$

We note that the lapse function, α , obtained in this method is always negative near the puncture. In the

numerical simulation, we modify the initial condition for α appropriately and ensure its positivity.

For solving the momentum constraint, we decompose \hat{A}_{ij} as

$$\hat{A}_{ij} = \hat{\nabla}_i W_j + \hat{\nabla}_j W_i - \frac{2}{3} f_{ij} \hat{\nabla}_k W^k + K_{ij}^P, \quad (11)$$

where W_i is an auxiliary three-vector field, and $W^i = f^{ij} W_j$. K_{ij}^P denotes a conformally weighted extrinsic curvature associated with the linear momentum of the BH, written by [36]

$$K_{ij}^P = \frac{3}{2r_{\text{BH}}^2} [l_i P_j^{\text{BH}} + l_j P_i^{\text{BH}} - (f_{ij} - l_i l_j) l^k P_k^{\text{BH}}], \quad (12)$$

where $l^i = x_{\text{BH}}^i / r_{\text{BH}}$ is a unit radial vector, $l_i = f_{ij} l^j$, and P_i^{BH} is the linear momentum of the BH, which is determined by the condition in which the total linear momentum of the system should vanish,

$$P_i^{\text{BH}} = - \int j_i \psi^6 d^3x. \quad (13)$$

W_i obeys an elliptic equation

$$\Delta W_i + \frac{1}{3} \hat{\nabla}_i \hat{\nabla}_j W^j = 8\pi \psi^6 j_i, \quad (14)$$

which is derived by taking a derivative of Eq. (11) and using the momentum constraint.

To summarize, we solve the elliptic equations for ϕ , β^i , η , and W_i imposing outer boundary conditions derived from the asymptotic flatness. In the present formalism, we do not have to impose inner boundary conditions at the BH horizon unlike in the excision method [14, 15].

The basic equations for the hydrostatic equilibrium are derived from the condition of irrotation, i.e., the zero relativistic vorticity

$$\begin{aligned} \omega_{\mu\nu} &= \nabla_\mu(hu_\nu) - \nabla_\nu(hu_\mu) \\ &= 0, \end{aligned} \quad (15)$$

and from the helical symmetric relation for the specific momentum of the fluid $\mathcal{L}_\xi(hu^\mu) = 0$. One result is the first integral of the relativistic Euler equation,

$$h\xi_\mu u^\mu = -C (= \text{const}). \quad (16)$$

This equation determines h (and subsequently ρ , ε , and P through an EOS) for an arbitrarily chosen constant C . The irrotational flow condition implies the presence of a velocity potential Ψ , which determines the four-velocity of the fluid by $hu_i = D_i \Psi$, where D_i is the covariant derivative associated with γ_{ij} . The continuity equation $\nabla_\mu(\rho u^\mu) = 0$ then leads to an elliptic equation for the velocity potential Ψ .

A quasiequilibrium state is computed using an iteration method described in detail in [17]. During the iteration, we fix the center of mass of the binary with a 3PN-J condition described in [17, 24]; we determine the

center of mass phenomenologically so that the total angular momentum of the binary for a given value of Ωm_0 agrees with that derived by the third post-Newtonian (3PN) approximation [37]. In this condition, the initial orbital eccentricity is by a factor of ~ 2 smaller than that in other conditions tried to this time [18–20], and the eccentricity at the onset of the merger becomes $\lesssim 1\%$ for a longterm simulation which tracks ~ 5 inspiral orbits.

B. Piecewise polytropic equation of state

The temperature of NSs, except for newly born ones, are believed to be much lower than the Fermi energy of the constituent particles [38]. This implies that we can safely neglect the thermal effects and employ a cold EOS, for which the pressure, P , the specific internal energy, ε , and other thermodynamical quantities are written as a function of the rest-mass density ρ . One of the simplest cold EOSs is a polytropic EOS,

$$P = \kappa \rho^{1+1/n_p}, \quad (17)$$

where κ is the polytropic constant and $n_p (\geq 0)$ the polytropic index: In the following, we often refer to the adiabatic index defined by $\Gamma = 1 + 1/n_p$. The first law of the thermodynamics,

$$d\varepsilon = -Pd\left(\frac{1}{\rho}\right), \quad (18)$$

determines the specific internal energy as $\varepsilon = P/[(\Gamma-1)\rho]$ where we assume $\varepsilon = 0$ at $\rho = 0$. Then, the specific enthalpy h becomes

$$h = 1 + \kappa \frac{\Gamma}{\Gamma-1} \rho^{\Gamma-1}. \quad (19)$$

A piecewise polytropic EOS is a phenomenologically parametrized EOS, which reproduces cold nuclear-theory-based EOSs at high density only with a small number of polytropic constants and indices [11, 26, 27], i.e.,

$$P(\rho) = \kappa_i \rho^{\Gamma_i} \quad \text{for } \rho_{i-1} \leq \rho < \rho_i \quad (1 \leq i \leq n), \quad (20)$$

where n is the number of the pieces used to parametrize an EOS and ρ_i denote boundary densities for which we provide an appropriate value (see the method below). Here, $\rho_0 = 0$ and $\rho_n \rightarrow \infty$. κ_i is the polytropic constant and Γ_i the adiabatic index for each piece. We note that we could in principle match to the known more realistic EOS at lower density. However, using a single polytrope for the low-density EOS is justified to the extent that the radius and deformability of the NS as well as resulting gravitational waveforms in the merger phase are insensitive to the low-density EOS.

At each boundary density, $\rho = \rho_i$ ($i = 1, \dots, n-1$), the pressure is required to be continuous, i.e., $\kappa_i \rho_i^{\Gamma_i} = \kappa_{i+1} \rho_i^{\Gamma_{i+1}}$. Thus, if we give κ_1 , Γ_i , and ρ_i ($i = 1, \dots, n$),

the EOS is totally determined. For the zero-temperature EOS, the first law of the thermodynamics (18) holds, and thus, ε and h are also determined except for the choice of the integration constants, which are fixed by the continuity condition of ε (hence equivalently h) at each ρ_i .

Recently, several authors have shown that the piecewise polytropic EOS composed of one piece in the crust region and three pieces in the core region approximately reproduces most of nuclear-theory-based EOSs at high density [26]. Here, three pieces in the core region are required to reproduce a high-mass NS for which inner and outer cores could have different stiffness due to the variation of properties of high-density nuclear matter. In the present work, we pick up NSs of relatively low mass 1.2 – $1.35 M_\odot$, taking into account that the masses of the NSs in the observed binary are fairly small [39]. The highest density of such NSs is not high enough in general that the EOS for the high-density part plays a critical role (note that if the EOS is very soft, the EOS for the high-density region is important, but we do not pursue this possibility in this paper). An additional fact to be noted is that NSs in BH-NS binaries never achieve the state of density higher than the initial value; their density should decrease due to the tidal field of the companion BH during the evolution. For these reasons, we employ a simple version of piecewise polytropic EOS in this paper, in which only one piece is assigned for the core region and one piece for the crust region as in [11]. Following [11], we employ the parameters of the crust EOS for all the models as follows:

$$\Gamma_1 = 1.35692395, \quad (21)$$

$$\kappa_1/c^2 = 3.99873692 \times 10^{-8} \text{g}^{1-\Gamma_1} \text{cm}^{3\Gamma_1-3}. \quad (22)$$

On the other hand, we vary the value of Γ_2 (the adiabatic index for the core EOS). Authors in [11] propose that instead of giving the density ρ_1 , the pressure p at the fiducial density $\rho_{\text{fidu}} = 10^{14.7} \text{g/cm}^3$ in the core region should be provided because this parameter p is closely correlated with the NS radius and deformability [40]. Thus, we have the following relations:

$$p = \kappa_2 \rho_{\text{fidu}}^{\Gamma_2}, \quad (23)$$

$$\kappa_1 \rho_1^{\Gamma_1} = \kappa_2 \rho_1^{\Gamma_2} (= P(\rho_1)). \quad (24)$$

These determine the values of κ_2 and ρ_1 .

Table I lists the parameters of the EOSs employed in this paper, and several key quantities for each EOS. “2H,” “H,” “HB,” and “B” denote very stiff, stiff, moderately stiff, and soft EOSs, respectively, for which $\Gamma_2 = 3.0$ universally, but the values of p are varied [11]. For “HB,” “HBs,” and “HBss” or “B,” “Bs,” and “Bss,” we assign the same value of p but different values of Γ_2 . The subscript “s” denotes that the value of Γ_2 is smaller. For “s” and “ss,” $\Gamma_2 = 2.7$ and 2.4 , respectively.

We calculate all the physical quantities for the spherical NS in equilibrium both by solving the Tolman-Oppenheimer-Volkoff equation directly and using the

code to calculate initial conditions in the isotropic gauge by LORENE, and check that numerical values agree with each other within 0.03%. Figure 1 plots the relation between the mass M_{NS} and circumferential radius R_{NS} for the spherical NSs with the adopted piecewise polytropic EOSs. For comparison, we also plot the relation for $\Gamma = 2$ polytropic EOS with $\kappa/c^2 = 2 \times 10^{-16} \text{g}^{-1} \text{cm}^3$. Note that in the polytropic EOS with a fixed adiabatic index, only the shape of this relation has an invariant meaning and there is a freedom of the absolute scaling, since all the dimensional quantities can be rescaled through the polytropic length scale $R_{\text{poly}} \equiv \kappa^{1/(2\Gamma-2)}$.

Figure 1 shows that for a given mass $\sim 1.35M_{\odot}$, the radius depends strongly on the EOSs, whereas the radius for a given piecewise polytropic EOS depends only weakly on the mass around the canonical mass $\sim 1.35M_{\odot}$. This weak dependence of the radius on the mass is an often-seen feature for the nuclear-theory-based EOSs [38]. By contrast, the relation calculated with the $\Gamma = 2$ polytropic EOS does not show this feature. Figure 1 illustrates that the dependence of the radius R_{NS} on the mass M_{NS} becomes much stronger in this EOS than in the piecewise polytropic EOSs. This illustrates that the $\Gamma = 2$ polytropic EOS is not very realistic.

Comparison of the quantities among HB, HBs, and HBss EOS models in Table I reveals a complicated mass-radius relation: HB is not always stiffer than HBss. Indeed, the radius with $M_{\text{NS}} = 1.2M_{\odot}$ is largest for HBss and smallest for HB among three models, whereas the radius with $M_{\text{NS}} = 1.35M_{\odot}$ is largest for HB and smallest for HBss. This complicated relation of the “stiffness” is due to the choice for the combination (Γ_2, p) (cf. Table I). For a density smaller than ρ_{fidu} , HBss EOS is stiffer than HB and HBs EOSs, whereas for a high density $\rho > \rho_{\text{fidu}}$, HB EOS is stiffer than the others. For a given high-mass NS for which the central density is much larger than ρ_{fidu} , the radius with HB EOS should be larger than that with other two EOSs. By contrast, for a given low-mass NS for which the central density is not very high, the radius with HB EOS should be smallest.

C. Models

The previous works by three groups [22–24] have found that the NSs in BH-NS binaries with high mass ratio $Q \gtrsim 4$ are barely subject to tidal disruption if the companion BH is not spinning: At the merger, the BH swallows most of the NS matter at one moment and the remnant disk mass is quite small or nearly equal to zero. Namely, the NS behaves approximately as a point particle even at the ISCO. Gravitational waves emitted in such a case have a similar waveform to that from a BH-BH binary. Because the behavior of NSs with high-mass BH companions does not show remarkable dependence on the EOS, they are unsuitable for the purpose of this paper, i.e., to investigate the effect of the EOS on gravitational waves and final outcomes. Thus, we focus only

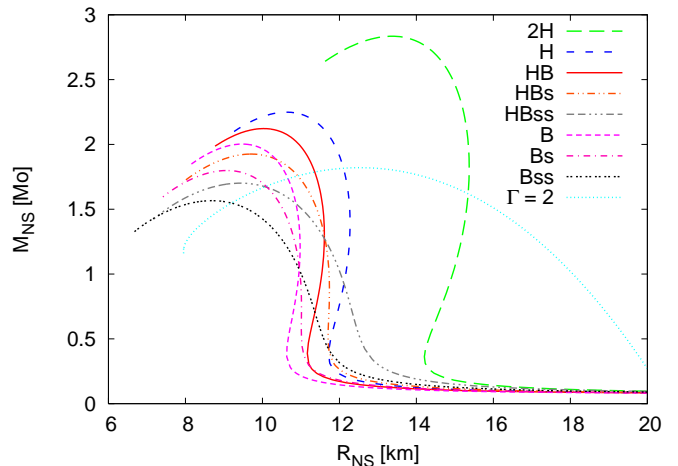


FIG. 1. The relation between the mass and circumferential radius of the spherical NSs for piecewise polytropic EOSs adopted in this paper. For comparison, we also plot the curve for $\Gamma = 2$ polytropic EOS with $\kappa/c^2 = 2 \times 10^{-16} \text{g}^{-1} \text{cm}^3$ (dotted curve).

on low mass-ratio binaries with $Q = 2$ and 3 in this paper. Also, we choose relatively low-mass NSs, because two-piece EOSs adopted in this paper may not be appropriate for modeling a high-mass NS with high central density, due to the lack of model parameters in the high-density region.

Table II summarizes key quantities for the initial models employed in the present numerical simulation. The labels for the models denote the name of the EOS, the mass ratio, and the NS mass; e.g., 2H-Q2M135 is modeled by 2H EOS, and its mass ratio and the NS mass are 2 and $1.35M_{\odot}$, respectively. The primary purpose of this paper is to study the dependence of gravitational waveforms and the final outcome on (i) the EOS of NSs, (ii) the mass ratio, and (iii) the NS mass. These purposes are reflected in our choice of the initial models.

We prepare quasiequilibrium states basically with the same value of Ωm_0 for the same value of Q irrespective of the EOS. The value of Ωm_0 is chosen to be small enough that the binaries spend more than 5 inspiral orbits before the onset of the merger. For $Q = 2$ binaries, a smaller value of initial angular velocity is required only for 2H EOS, because the NS with this EOS has a much larger radius than with other EOSs and is sensitive to the BH tidal force even for a larger orbital separation; to track $\gtrsim 5$ inspiral orbits before the tidal disruption, we have to choose the value of Ωm_0 by $\sim 10\%$ as small as that for other EOSs. For the case of $Q = 3$, we also choose smaller values of Ωm_0 for $M_{\text{NS}} = 1.2M_{\odot}$ cases.

III. METHODS OF SIMULATIONS

Numerical simulation is performed using an adaptive-mesh refinement (AMR) code SACRA [41]. The formu-

TABLE I. Key ingredients of the adopted EOSs. Γ_2 is the adiabatic index in the core region and p is the pressure at the fiducial density $\rho_{\text{fidu}} = 10^{14.7} \text{ g/cm}^3$, which determines the polytropic constant κ_2 of the core region and ρ_1 : the critical rest-mass density separating the crust and core regions. M_{max} is the maximum mass of the NS for a given EOS. R_{135} (R_{12}) and \mathcal{C}_{135} (\mathcal{C}_{12}) are the circumferential radius and the compactness of the NS with $M_{\text{NS}} = 1.35M_{\odot}$ ($1.2M_{\odot}$).

| Model | Γ_2 | $\log_{10} p \text{ (g/cm}^3\text{)}$ | $\rho_1 \text{ (10}^{14} \text{ g/cm}^3\text{)}$ | $M_{\text{max}}[M_{\odot}]$ | $R_{135} \text{ (km)}$ | \mathcal{C}_{135} | $R_{12} \text{ (km)}$ | \mathcal{C}_{12} |
|-------|------------|---------------------------------------|--|-----------------------------|------------------------|---------------------|-----------------------|--------------------|
| 2H | 3.0 | 13.95 | 0.7033 | 2.835 | 15.23 | 0.1309 | 15.12 | 0.1172 |
| H | 3.0 | 13.55 | 1.232 | 2.249 | 12.27 | 0.1624 | 12.25 | 0.1447 |
| HB | 3.0 | 13.45 | 1.417 | 2.122 | 11.61 | 0.1718 | 11.60 | 0.1527 |
| HBs | 2.7 | 13.45 | 1.069 | 1.926 | 11.57 | 0.1723 | 11.67 | 0.1519 |
| HBss | 2.4 | 13.45 | 0.6854 | 1.701 | 11.45 | 0.1741 | 11.74 | 0.1509 |
| B | 3.0 | 13.35 | 1.630 | 2.003 | 10.96 | 0.1819 | 10.98 | 0.1614 |
| Bs | 2.7 | 13.35 | 1.269 | 1.799 | 10.74 | 0.1856 | 10.88 | 0.1629 |
| Bss | 2.4 | 13.35 | 0.8547 | 1.566 | 10.27 | 0.1940 | 10.66 | 0.1663 |

TABLE II. Key parameters and quantities for the initial conditions adopted in the numerical simulations. The adopted EOS, mass ratio (Q), NS mass in isolation (M_{NS}), angular velocity (Ω) in units of c^3/Gm_0 , baryon rest mass (M_*), compactness of the NS in isolation (\mathcal{C}), maximum rest-mass density (ρ_{max}), ADM mass of the system (M_0), and total angular momentum of the system (J_0), respectively.

| Model | EOS | Q | $M_{\text{NS}}[M_{\odot}]$ | $G\Omega m_0/c^3$ | $M_*[M_{\odot}]$ | \mathcal{C} | $\rho_{\text{max}} \text{ (g/cm}^3\text{)}$ | $M_0[M_{\odot}]$ | $J_0[GM_{\odot}^2/c]$ |
|-------------|------|-----|----------------------------|-------------------|------------------|---------------|---|------------------|-----------------------|
| 2H-Q2M135 | 2H | 2 | 1.35 | 0.0250 | 1.455 | 0.1309 | 3.740×10^{14} | 4.015 | 14.39 |
| H-Q2M135 | H | 2 | 1.35 | 0.0280 | 1.484 | 0.1624 | 7.018×10^{14} | 4.013 | 14.02 |
| HB-Q2M135 | HB | 2 | 1.35 | 0.0280 | 1.493 | 0.1718 | 8.262×10^{14} | 4.013 | 14.02 |
| HBs-Q2M135 | HBs | 2 | 1.35 | 0.0280 | 1.489 | 0.1723 | 9.154×10^{14} | 4.013 | 14.02 |
| HBss-Q2M135 | HBss | 2 | 1.35 | 0.0280 | 1.485 | 0.1741 | 1.082×10^{15} | 4.013 | 14.02 |
| B-Q2M135 | B | 2 | 1.35 | 0.0280 | 1.503 | 0.1819 | 9.761×10^{14} | 4.013 | 14.02 |
| Bs-Q2M135 | Bs | 2 | 1.35 | 0.0280 | 1.501 | 0.1856 | 1.137×10^{15} | 4.013 | 14.02 |
| Bss-Q2M135 | Bss | 2 | 1.35 | 0.0280 | 1.501 | 0.1940 | 1.490×10^{15} | 4.013 | 14.02 |
| 2H-Q3M135 | 2H | 3 | 1.35 | 0.0280 | 1.455 | 0.1309 | 3.737×10^{14} | 5.359 | 21.05 |
| H-Q3M135 | H | 3 | 1.35 | 0.0300 | 1.484 | 0.1624 | 7.011×10^{14} | 5.358 | 20.74 |
| HB-Q3M135 | HB | 3 | 1.35 | 0.0300 | 1.493 | 0.1718 | 8.254×10^{14} | 5.358 | 20.74 |
| B-Q3M135 | B | 3 | 1.35 | 0.0300 | 1.503 | 0.1819 | 9.751×10^{14} | 5.357 | 20.74 |
| 2H-Q2M12 | 2H | 2 | 1.20 | 0.0220 | 1.282 | 0.1172 | 3.466×10^{14} | 3.571 | 11.71 |
| H-Q2M12 | H | 2 | 1.20 | 0.0280 | 1.303 | 0.1447 | 6.421×10^{14} | 3.567 | 11.08 |
| HB-Q2M12 | HB | 2 | 1.20 | 0.0280 | 1.310 | 0.1527 | 7.522×10^{14} | 3.567 | 11.08 |
| B-Q2M12 | B | 2 | 1.20 | 0.0280 | 1.317 | 0.1614 | 8.832×10^{14} | 3.567 | 11.08 |
| HB-Q3M12 | HB | 3 | 1.20 | 0.0280 | 1.310 | 0.1527 | 7.517×10^{14} | 4.763 | 1.663 |
| B-Q3M12 | B | 3 | 1.20 | 0.0280 | 1.317 | 0.1614 | 8.826×10^{14} | 4.763 | 1.663 |

lation, the gauge conditions, the numerical scheme, and the methods of diagnostics are essentially the same as those described in [24, 41] except for the EOS. Thus, we here only briefly review them. We also describe the present setup of the computational domain for the AMR algorithm and grid resolution in Sec. III C.

A. Formulation and numerical methods

In SACRA, we solve Einstein's evolution equation in the BSSN formalism [42, 43] with the moving-puncture method [36, 44, 45]. We evolve a conformal factor $W \equiv \gamma^{-1/6}$, the conformal three-metric $\tilde{\gamma}_{ij} = \gamma^{-1/3}\gamma_{ij}$, the

trace of the extrinsic curvature K , the conformal trace-free part of the extrinsic curvature $\tilde{A}_{ij} = \gamma^{-1/3}(K_{ij} - K\gamma_{ij}/3)$, and an auxiliary variable $\tilde{\Gamma}^i \equiv -\partial_j \tilde{\gamma}^{ij}$. The spatial derivatives in the evolution equations are evaluated by a fourth-order centered finite difference except for the advection terms which is evaluated by a fourth-order non-centered finite difference. A fourth-order Runge-Kutta method is employed for the time evolution.

Following [46], we employ a moving-puncture gauge in the form

$$(\partial_t - \beta^j \partial_j)\alpha = -2\alpha K, \quad (25)$$

$$(\partial_t - \beta^j \partial_j)\beta^i = (3/4)B^i, \quad (26)$$

$$(\partial_t - \beta^j \partial_j)B^i = (\partial_t - \beta^j \partial_j)\tilde{\Gamma}^i - \eta_s B^i, \quad (27)$$

where B^i is an auxiliary variable and η_s is an arbitrary constant. In this work, we typically set $\eta_s \approx M_\odot/M_{\text{BH}}$.

For the hydrodynamics, we evolve $\rho_* \equiv \rho \alpha u^t W^{-3}$, $\hat{u}_i \equiv h u_i$, and $e_* \equiv h \alpha u^t - P/(\rho \alpha u^t)$. To handle the advection terms, we adopt a high-resolution central scheme by Kurganov and Tadmor [47] with a third-order piecewise parabolic interpolation for the cell reconstruction.

With regards to the EOS, we decompose the pressure and the specific internal energy into cold and thermal parts as follows (e.g., [48])

$$P = P_{\text{cold}} + P_{\text{th}}, \quad \varepsilon = \varepsilon_{\text{cold}} + \varepsilon_{\text{th}}. \quad (28)$$

Here, the thermal part is nonzero only in the presence of shock heating, and thus, this part plays a role for the evolution only in the merger phase. Once the primitive variables ρ and ε are recovered from the conserved variables ρ_* , \hat{u}_i , and e_* , we calculate zero-temperature parts P_{cold} and $\varepsilon_{\text{cold}}$ from ρ using the piecewise polytropic EOS (20). Then, the thermal part of the specific internal energy is calculated by $\varepsilon_{\text{th}} = \varepsilon - \varepsilon_{\text{cold}}$, and finally the thermal part of the pressure P_{th} is determined. In this paper, we adopt a simple Γ -law, ideal-gas EOS for the thermal part as (e.g., [48])

$$P_{\text{th}} = (\Gamma_{\text{th}} - 1)\rho\varepsilon_{\text{th}}, \quad (29)$$

where Γ_{th} is an adiabatic index for the thermal part. We choose Γ_{th} equal to the adiabatic index in the crust region, Γ_1 , for simplicity.

Because the vacuum is not allowed in any conservative hydrodynamic scheme, an artificial atmosphere of small density is distributed outside the NS in the same manner as done in our previous work [24]. The rest-mass density of the atmosphere is set to be $\rho_{\text{atm}} = 10^{-9}\rho_{\text{max}} \approx 10^6 \text{ g/cm}^3$ for the inner computational domain. For the outer domain with $r \geq r_c \approx 20R_{\text{NS}}$, a smaller density is assigned according to the rule $\rho = \rho_{\text{atm}}e^{1-r/r_c}$. The total rest mass of the atmosphere is always less than $10^{-5}M_\odot$, and hence, we can safely neglect spurious effects by accretion of the atmosphere onto the remnant accretion disk as long as the disk mass is much larger than $10^{-5}M_\odot$.

B. Diagnostics

Gravitational waves are extracted calculating the outgoing part of the complex Weyl scalar Ψ_4 , which we eval-

uate at a finite coordinate radii $r = 300\text{--}400M_\odot$. Gravitational waveforms are obtained by integrating Ψ_4 twice in time as

$$h_+(t) - ih_\times(t) = - \int^t dt' \int^{t'} dt'' \Psi_4(t''), \quad (30)$$

and then by subtracting the quadratic function $a_2 t^2 + a_1 t + a_0$ from the obtained waveform using the least-square fitting for determining the constants a_0 , a_1 , and a_2 . The purpose of this subtraction is to eliminate unphysical components in numerically calculated Weyl scalar, Ψ_4 [49], as described in [24] (see also [50]). We also calculate the amount of radiated energy ΔE and angular momentum ΔJ by integrating the emission rate calculated from the Weyl scalar Ψ_4 as

$$\frac{dE}{dt} = \frac{r^2}{16\pi} \oint_S \left| \int \Psi_4 dt \right|^2 dA, \quad (31)$$

$$\frac{dJ_z}{dt} = -\frac{r^2}{16\pi} \text{Re} \left[\oint_S \left(\int \bar{\Psi}_4 dt \right) \times \left(\int \int \partial_\varphi \Psi_4 dt dt' \right) dA \right], \quad (32)$$

where S denotes a coordinate sphere of $r = \text{const}$, $dA = r^2 d(\cos\theta) d\varphi$ is the surface element of S , and $\bar{\Psi}_4$ is the complex conjugate of Ψ_4 . We decompose Ψ_4 into $s = -2$ spin-weighted spherical harmonics of $2 \leq l \leq 4$. Among them, $(l, |m|) = (2, 2)$ modes are always dominant but higher l modes such as $(l, |m|) = (3, 3)$, $(4, 4)$ and $(2, 1)$ modes contribute to the totally radiated energy and angular momentum by larger than 1%.

We compare numerical waveforms with those derived by the Taylor-T4 formula in the post-Newtonian approximation [51] for two point masses in quasicircular orbits. Assuming that both the BH and NS have no spin angular momentum, we calculate the evolution of the orbital angular velocity $\Omega(t)$ through $X(t) = [m_0 \Omega(t)]^{2/3}$ and the orbital phase $\Theta(t)$ up to 3.5PN order by solving the ordinary differential equations [52]

$$\begin{aligned} \frac{dX}{dt} = & \frac{64\nu X^5}{5m_0} \left[1 - \frac{743 + 924\nu}{336} X + 4\pi X^{3/2} + \left(\frac{34103}{18144} + \frac{13661}{2016}\nu + \frac{59}{18}\nu^2 \right) X^2 \right. \\ & - \left(\frac{4159}{672} + \frac{15876}{672}\nu \right) \pi X^{5/2} + \left\{ \frac{16447322263}{139708800} - \frac{1712}{105}\gamma_E + \frac{16}{3}\pi^2 - \left(\frac{56198689}{217728} - \frac{451}{48}\pi^2 \right) \nu \right. \\ & \left. \left. + \frac{541}{896}\nu^2 - \frac{5605}{2592}\nu^3 - \frac{856}{105} \ln(16X) \right\} X^3 - \left(\frac{4415}{4032} - \frac{358675}{6048}\nu - \frac{91495}{1512}\nu^2 \right) \pi X^{7/2} \right], \end{aligned} \quad (33)$$

$$\frac{d\Theta}{dt} = \frac{X^{3/2}}{m_0}, \quad (34)$$

where $\nu = Q/(1+Q)^2$ and γ_E is the Euler constant.

After X and Θ are obtained, we calculate complex gravitational-wave amplitude h^{22} of $(l, m) = (2, 2)$ mode, assuming that the binary is orbiting on the equatorial ($\theta = \pi/2$) plane, up to 3PN order using the formula [53]

$$\begin{aligned} h^{22} = & -8\sqrt{\frac{\pi}{5}} \frac{\nu m_0}{D} e^{-2i\Theta} X \left[1 - \left(\frac{107}{42} - \frac{55}{42}\nu \right) X + 2\pi X^{3/2} - \left(\frac{2173}{1512} + \frac{1069}{216}\nu - \frac{2047}{1512}\nu^2 \right) X^2 \right. \\ & - \left\{ \left(\frac{107}{21} - \frac{34}{21}\nu \right) \pi + 24i\nu \right\} X^{5/2} + \left\{ \frac{27027409}{646800} - \frac{856}{105}\gamma_E + \frac{2}{3}\pi^2 - \frac{1712}{105} \ln 2 - \frac{428}{105} \ln X \right. \\ & \left. \left. - \left(\frac{278185}{33264} - \frac{41}{96}\pi^2 \right) \nu - \frac{20261}{2772}\nu^2 + \frac{114635}{99792}\nu^3 + \frac{428}{105}i\pi \right\} X^3 \right], \end{aligned} \quad (35)$$

where D is a distance between the binary and an observer. We also compute a gravitational-wave spectrum from the waveform obtained in this way.

We determine the properties of the BHs formed after the merger such as masses and spins using the quantities associated with the apparent horizon. The apparent horizon is determined in the same manner as described in [41].

The BH mass may be estimated by two methods. In the first method, we measure the circumferential radius C_e of the apparent horizon along the equatorial plane and calculate $C_e/4\pi$, which gives the BH mass in the stationary vacuum BH spacetime. By this method, we estimate the mass of the remnant BH after the spacetime settles to an approximately steady state (assuming that deviation from Kerr spacetime due to the presence of surrounding materials is negligible). In the second method, we measure the irreducible mass of the BH, M_{irr} , which is determined from the area of the apparent horizon A_{AH} as

$$M_{\text{irr}} = \sqrt{\frac{A_{\text{AH}}}{16\pi}}. \quad (36)$$

For the Kerr spacetime, M_{irr} is written by the mass and dimensionless spin parameter $a \equiv J_{\text{BH}}/M_{\text{BH}}^2$ of a BH (where J_{BH} is the spin angular momentum of the BH) as

$$M_{\text{irr}} = M_{\text{BH}} \sqrt{\frac{1 + \sqrt{1 - a^2}}{2}}. \quad (37)$$

Thus, if either the BH spin or mass is known, the BH mass or spin is determined (again assuming that deviation from Kerr spacetime due to the presence of surrounding materials is negligible). For the Kerr spacetime, this relation may be written as

$$M_{\text{irr}} = \frac{C_e}{4\sqrt{2}\pi} \sqrt{1 + \sqrt{1 - a^2}}. \quad (38)$$

Thus, we may say that the spin is estimated by calculating M_{irr} and C_e .

The dimensionless spin parameter of the BH is estimated also using the quantities defined on the apparent horizon. For a Kerr BH with spin parameter a , the ratio of the circumferential radius along the meridional plane C_p to the one along the equatorial plane C_e is written as

$$\frac{C_p}{C_e} = \frac{\sqrt{2\hat{r}_+}}{\pi} E\left(\frac{a^2}{2\hat{r}_+}\right), \quad (39)$$

where $\hat{r}_+ = 1 + \sqrt{1 - a^2}$ is the normalized radius of the horizon and $E(z)$ is an elliptic integral

$$E(z) = \int_0^{\pi/2} \sqrt{1 - z \sin^2 \theta} d\theta. \quad (40)$$

Assuming that this relation holds for a BH surrounded by materials again, we estimate the spin parameter of the remnant BH.

Comparison of the spin obtained from C_p/C_e with that derived from Eq. (38) provides a consistency check. It is found that these two values agree with each other within the error $\Delta a = 0.003$ irrespective of the model of BH-NS binaries. For this reason, in the following, we only present the spin determined from C_p/C_e .

In addition to the quantities for the remnant BHs, we calculate the total rest mass of materials located outside the apparent horizon by integrating the rest-mass density with respect to the proper volume element,

$$M_{r>r_{\text{AH}}} \equiv \int_{r>r_{\text{AH}}} \rho_* d^3x, \quad (41)$$

where $r_{\text{AH}} = r_{\text{AH}}(\theta, \varphi)$ denotes the radius of the apparent horizon as a function of the angular coordinates (θ, φ) . $M_{r>r_{\text{AH}}}$ is regarded as the mass of the remnant disk when the system settles to a quasistationary state after the merger.

C. Setup of AMR grids

Numerical simulation is performed using an AMR algorithm described in [41], to which the reader may refer

TABLE III. Setup of the grid structure for the computation with our AMR algorithm. $\Delta x = h_6 = L/(2^6 N)$ is the grid spacing at the finest-resolution domain with L being the location of the outer boundaries for each axis. $R_{\text{diam}}/\Delta x$ denotes the grid number assigned inside the semimajor diameter of the NS. λ_0 is the gravitational wavelength of the initial configuration.

| Model | $\Delta x/M_0$ | $R_{\text{diam}}/\Delta x$ | L/λ_0 |
|-------------|----------------|----------------------------|---------------|
| 2H-Q2M135 | 0.0471 | 90.8 | 1.189 |
| H-Q2M135 | 0.0377 | 86.2 | 1.065 |
| HB-Q2M135 | 0.0347 | 87.0 | 0.982 |
| HBs-Q2M135 | 0.0353 | 85.2 | 0.998 |
| HBss-Q2M135 | 0.0353 | 84.0 | 0.998 |
| B-Q2M135 | 0.0330 | 85.1 | 0.932 |
| Bs-Q2M135 | 0.0324 | 84.4 | 0.915 |
| Bss-Q2M135 | 0.0270 | 95.4 | 0.825 |
| 2H-Q3M135 | 0.0353 | 89.0 | 0.998 |
| H-Q3M135 | 0.0282 | 84.7 | 0.856 |
| HB-Q3M135 | 0.0269 | 82.7 | 0.816 |
| B-Q3M135 | 0.0247 | 83.8 | 0.749 |
| 2H-Q2M12 | 0.0565 | 86.9 | 1.255 |
| H-Q2M12 | 0.0453 | 83.1 | 1.281 |
| HB-Q2M12 | 0.0420 | 83.6 | 1.188 |
| B-Q2M12 | 0.0392 | 83.4 | 1.109 |
| HB-Q3M12 | 0.0306 | 84.6 | 0.866 |
| B-Q3M12 | 0.0278 | 86.9 | 0.786 |

for details. In the present work, we prepare seven refinement levels to ensure that the computational domain extends to the local wave zone for initial quasiequilibrium states and that both compact objects are resolved with a sufficient grid resolution (e.g., Table III). Each refinement domain consists of the uniform, vertex-centered grids with $(2N+1, 2N+1, N+1)$ grid points for (x, y, z) with the equatorial plane symmetry at $z=0$ imposed. In the present work, we typically choose $N=50$, with the exception that $N=54$ for model Bss-Q2M135, in which the NS is quite compact and needs to be resolved with a better grid resolution. For several models arbitrarily chosen, we performed numerical simulations with lower grid resolutions, $N=36$ and 42 , to check the convergence of the numerical results (see the Appendix). The edge length of the largest domain is denoted by $2L$ and the grid spacing for each domain is then $h_l = L/(2^l N)$, where $l=0-6$. In all the simulations, two sets of four finer domains comoving with compact objects cover the region in the vicinity of two objects, and the other three coarser domains cover both objects by a wider domain with their origins being fixed at the approximate center of mass of the binary. Namely, we prepare 11 refinement domains in total for all the simulations.

Table III summarizes the parameters of the grid structure for the simulations in this paper. As mentioned above, the value of L is chosen to be $\approx \lambda_0$, where

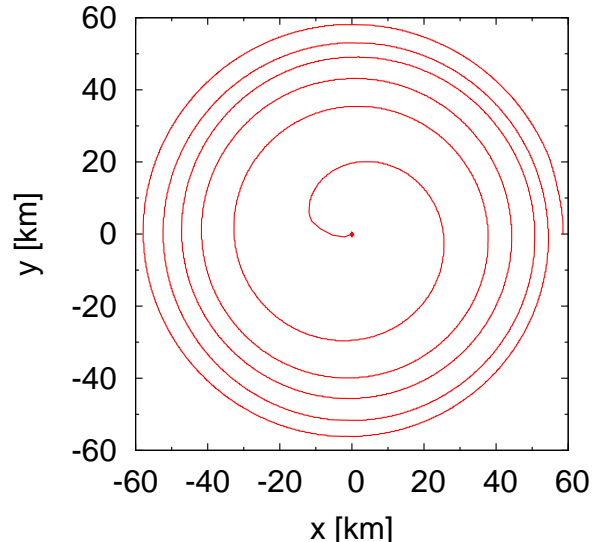


FIG. 2. Evolution of the coordinate separation of the binary x_{sep}^i for model HB-Q2M135.

$\lambda_0 \equiv \pi/\Omega_0$ is the gravitational wavelength at $t=0$ and Ω_0 is the orbital angular velocity of the initial configuration. Because the gravitational wavelength decreases during the evolution of the binaries, the outer boundary of the computational domains is guaranteed to be located in the wave zone throughout the simulation. Each of the two finest domains covers the semimajor axis of the NS with 42–48 grid points and the BH radius (the coordinate radius of the apparent horizon) with typically ≈ 20 grid points, respectively. For $N=54$ run, the total memory required for the simulations is about 11.6 G bytes. We perform numerical simulations with personal computers of 12 G bytes memory and of core-i7X processors with clock speed 3.2 or 3.33 GHz. We only use two processors to perform one job with an OPEN-MP library. Typical computational time required to perform one simulation (for ~ 40 ms in physical time of coalescence) is 7–10 weeks.

IV. NUMERICAL RESULTS

A. Orbital evolution and general merger process

To obtain a realistic numerical result for gravitational waveforms and the final outcome formed after the merger, it is necessary to exclude spurious effects associated with a noncircularity in the orbital motion as much as possible. To assess the circularity of the orbital motion, we plot the evolution of the coordinate separation $x_{\text{sep}}^i = x_{\text{NS}}^i - x_{\text{BH}}^i$ for model HB-Q2M135 in Fig. 2. Here, the position of the maximum rest-mass density is identified as the coordinate of the NS, x_{NS}^i , and the location of the puncture, x_{P}^i , is the coordinate of the BH, x_{BH}^i .

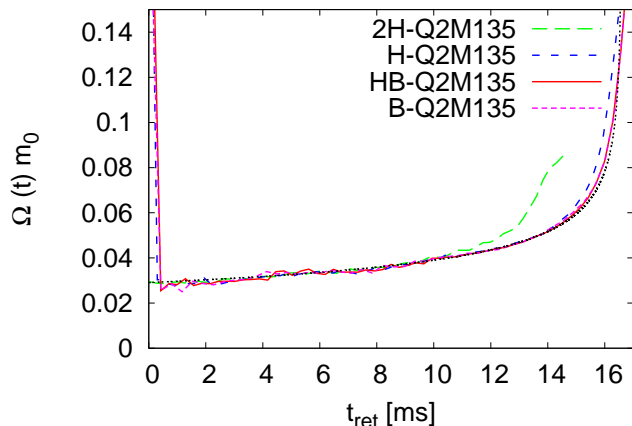


FIG. 3. Time evolution of the orbital angular velocity $\Omega(t)m_0$ for models 2H-Q2M135, H-Q2M135, HB-Q2M135, and B-Q2M135 as a function of a retarded time defined by Eq. (43) with an appropriate time shift. The dotted curve denotes the evolution of the orbital angular velocity calculated by the Taylor-T4 formula.

This figure suggests that the orbital eccentricity appears to be low throughout the whole evolution. Because $\gtrsim 5$ orbits are tracked, the eccentricity, which is likely to be nonzero initially, should be suppressed by gravitational radiation reaction. We note that for all the models, similar trajectories are found.

The coordinate separation shown above is a gauge-dependent quantity. To show a stronger evidence that the eccentricity is suppressed to a small level, it is better to plot a gauge-independent quantity. Figure 3 plots the evolution of the orbital angular velocity defined from the $(l, m) = (2, 2)$ mode of Ψ_4 by

$$\Omega(t) = \frac{1}{2} \frac{|\Psi_4(l=m=2)|}{|\int \Psi_4(l=m=2)dt|}, \quad (42)$$

for models 2H-Q2M135, H-Q2M135, HB-Q2M135, and B-Q2M135. Here, the horizontal axis is chosen to be an approximate retarded time defined by

$$t_{\text{ret}} = t - D - 2M_0 \ln(D/M_0). \quad (43)$$

We here do not plot the curve after the onset of tidal disruption. For comparison, the angular velocity derived from the Taylor-T4 formula is also plotted. To align the curve in the inspiral phase for $\Omega(t)m_0 \leq 0.05$, we appropriately shift the time for each model. For $t_{\text{ret}} \lesssim 0$ ms, an unphysical (a junk wave) component contained in the initial data dominates the waveform, and hence, $\Omega(t)$ derived from Eq. (42) does not give the angular velocity.

Figure 3 shows that the angular velocity obtained in numerical simulations agrees with that by the Taylor-T4 formula within a small modulation of $\Delta\Omega/\Omega \lesssim 5\%$ irrespective of the models. With the fact that the orbital eccentricity is approximately estimated as $e \approx 2\Delta\Omega/3\Omega$

for $e \ll 1$, we conclude that the orbital eccentricity is suppressed within $\sim 3\%$. Figure 3 also shows that the deviation from the Taylor-T4 result becomes remarkable in an earlier time for models with stiffer EOSs such as 2H and H EOSs. This is due to the fact that the tidal elongation and disruption of the NS occur at slightly earlier stages of the inspiral orbits for models with the stiffer EOSs. This illustrates the fact that the stiffness of the EOS is reflected clearly in the gravitational-wave frequency (and gravitational-wave phase) as a function of time.

Figures 4 and 5 plot the snapshots of the rest-mass density profiles and the location of the apparent horizon on the equatorial plane at selected time slices for models 2H-Q2M12 and B-Q3M135. Figure 4 illustrates the process in which the NS is tidally disrupted to form a disk surrounding the companion BH. In this case, the NS is disrupted far outside the ISCO and then forms a one-armed spiral arm with large angular momentum. As a consequence of the angular momentum transport in the arm, a large amount of materials spread outward and then form a disk around the BH. We will report more details about the remnant disk in Sec. IV D. Figure 5 illustrates the case in which the NS is not tidally disrupted before it is swallowed by the BH. In this case, mass of the disk formed after the onset of the merger is negligibly small.

B. Gravitational waveforms

Figures 6 and 7 plot the $(l, m) = (2, 2)$, plus-mode gravitational waveforms obtained numerically (hereafter referred to as h_+). All the waveforms are shown for an observer located along the z axis (axis perpendicular to the orbital plane) and plotted as a function of a retarded time t_{ret} . We plot the amplitude in a normalized form, Dh_+/m_0 , and the physical amplitude observed by an observer located at a hypothetical distance $D = 100$ Mpc.

To validate the numerical waveforms, we compare them with the Taylor-T4 waveform, which is accurate up to 3.5PN order in phase and 3PN order in amplitude, with an appropriate time shift; the time shift is carried out to align the curve of $\Omega(t)$ as performed in Sec. IV A. Figures 6 and 7 show that these two waveforms agree with each other irrespective of models during the inspiral phase, except for 2–3 initial cycles. The reasons for this initial disagreement are that an approaching velocity associated with gravitational radiation reaction is not taken into account in the initial data and also the initial condition does not exactly model a quasicircular state, because we do not fully solve Einstein's equation for deriving it.

The numerical waveforms in the merger phase also (but due to a physical reason) deviate from the Taylor-T4 ones both in phase and amplitude, in particular for models with stiff EOSs, e.g., 2H-Q2M135 and 2H-Q2M12. For such models, ringdown waveforms associated with the BH quasinormal mode are not seen in the merger

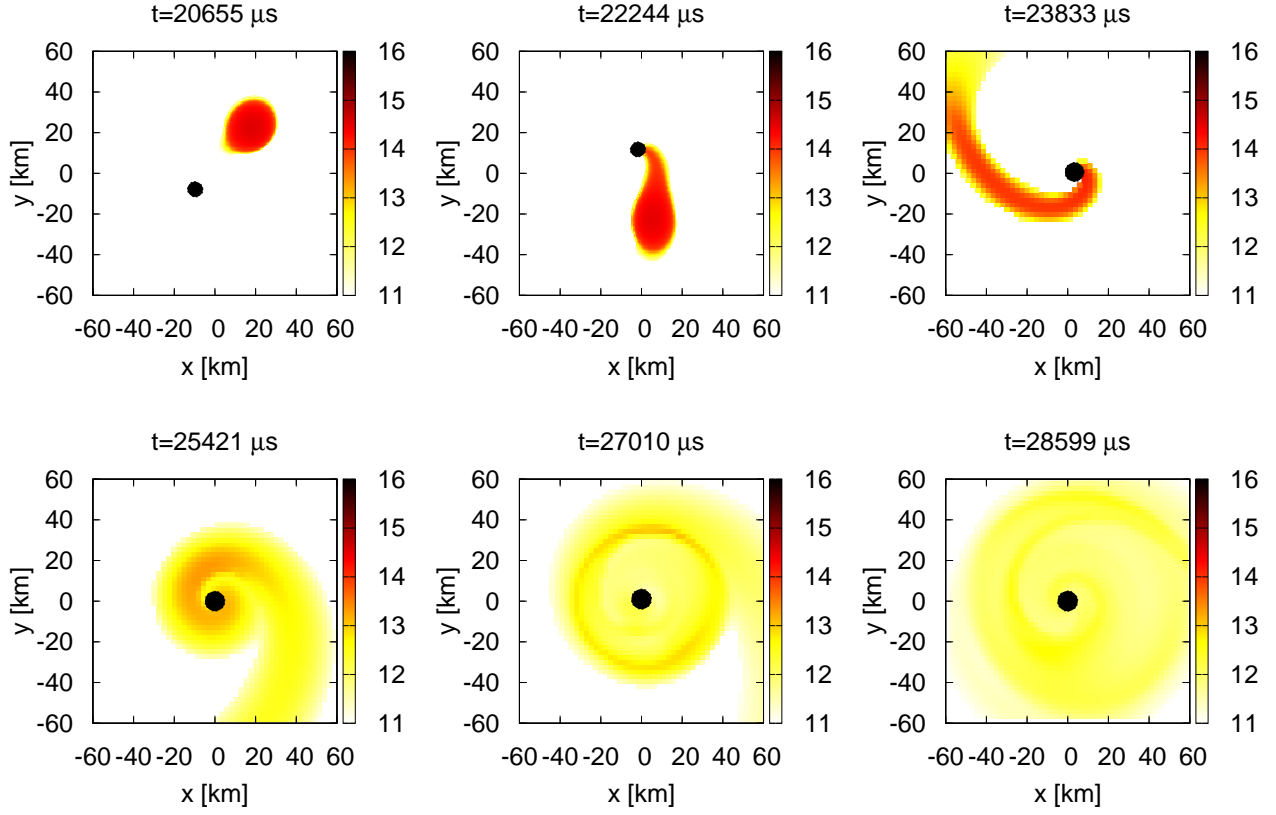


FIG. 4. Evolution of the rest-mass density profile in units of g/cm^3 and the location of the apparent horizon on the equatorial plane for model 2H-Q2M135. The filled circles denote the regions inside the apparent horizons. The color panels on the right-hand side of each figure show $\log_{10}(\rho)$.

and ringdown phases, and instead, the gravitational-wave amplitude damps suddenly in the middle of the inspiral phase. The reason for this quick damping is that the NS is tidally disrupted by the companion BH at an orbit in the inspiral phase within one orbital period, and then, the disrupted material forms a relatively low-density and nearly axisymmetric matter distribution around the BH, suppressing time variation of a mass quadrupole moment. Because the gravitational-wave emission stops in the middle of the inspiral motion, the maximum amplitude of gravitational waves is smaller for such a binary than for a binary with no tidal disruption, as shown in Fig. 6. All these facts illustrate that the finite size effect of the NS significantly modifies gravitational waves derived in the point-particle approximation (in the Taylor-T4 formula). On the other hand, ringdown gravitational waves are clearly seen for models with soft EOSs (for which tidal disruption does not occur) such as model B-Q3M135, in which the numerical and the Taylor-T4 waveforms are in more excellent agreement even in the late inspiral phase.

Table IV presents total radiated energy ΔE and angular momentum ΔJ carried away by gravitational waves. The contribution from all the $l = 2-4$ modes is taken into account for ΔE and ΔJ . We estimate systematic errors in the presented values to be less than 10%, which are associated mainly with the finite grid resolution and partly

with the finite extraction radii (cf. the Appendix). We note that the $(l, |m|) = (2, 2)$ modes always contribute by $\gtrsim 90\%$ to both for ΔE and ΔJ . The fraction of these modes is larger for binaries composed of less-compact NSs, because only binaries which escape the tidal disruption in the late inspiral phase can efficiently emit higher l -mode gravitational waves. Among other modes, $(3, 3)$ and $(4, 4)$ modes constitute most of the remaining part of ΔJ , whereas the order of magnitude of the $(2, 1)$ mode is as large as that of the $(4, 4)$ mode for ΔE .

The numerical results shown in Table IV illustrate a quantitative dependence of gravitational-wave emission on the compactness of the NS: For a given mass ratio, gravitational-wave emission continues for a longer duration and consequently total radiated energy and angular momentum are larger for binaries composed of more compact NSs. Comparison among the models with $Q = 2$ and $M_{\text{NS}} = 1.35M_{\odot}$ and with the same initial value of Ωm_0 shows that both $\Delta E/M_0$ and $\Delta J/J_0$ are monotonically increasing functions of the NS compactness \mathcal{C} . This point is also recognized from Figs. 6 and 7, e.g., from the comparison among gravitational waves for models H-Q2M135, HB-Q2M135, and B-Q2M135 (note that for model 2H-Q2M135 the simulation is started from a lower value of Ωm_0 and it is not suitable for this comparison). Table IV also shows that $\Delta J/\Delta E$ decreases as the EOS

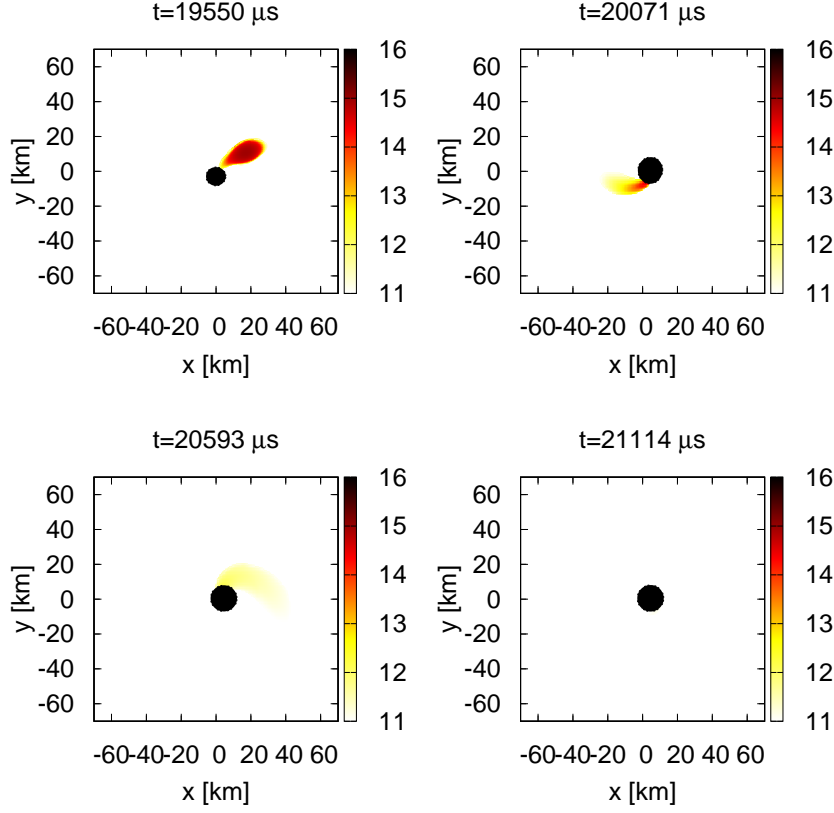


FIG. 5. The same as Fig. 4 but for model B-Q3M135.

softens. This is due to the fact that $\Delta J/\Delta E \approx m/\Omega$ for a given angular harmonic of m , and for a soft EOS, more radiation is emitted at large angular velocity, Ω .

C. Gravitational-wave spectrum

Characteristic features of a gravitational waveform, such as characteristic frequencies and their dependence on the EOS, are well reflected in the Fourier spectrum. Figures 8–10 display gravitational-wave spectra for all the models with the mass ratio $Q = 2$ and the models with the mass ratio $Q = 3$ and the NS mass $M_{\text{NS}} = 1.35M_{\odot}$. As before [24], we define the Fourier spectrum as a sum of each Fourier component of two independent polarizations of the $(l, m) = (2, 2)$ mode as

$$\tilde{h}(f) = \sqrt{\frac{|\tilde{h}_+(f)|^2 + |\tilde{h}_\times(f)|^2}{2}}, \quad (44)$$

$$\tilde{h}_A(f) = \int e^{2\pi i f t} h_A(t) dt, \quad (45)$$

where A denotes two polarization modes, $+$ or \times . In calculating $\tilde{h}(f)$ from a numerically obtained Weyl scalar, Ψ_4 , we always omit the unphysical radiation component extracted at $t_{\text{ret}} \lesssim 0$ ms using a step function of retarded time as the window function so that the

TABLE IV. Total radiated energy ΔE and angular momentum ΔJ carried away by gravitational waves. ΔE and ΔJ are normalized with respect to the initial ADM mass M_0 and angular momentum J_0 , respectively. We also show the ratio between ΔJ and ΔE .

| Model | $\Delta E/M_0(\%)$ | $\Delta J/J_0(\%)$ | $(\Delta J/J_0)/(\Delta E/M_0)$ |
|-------------|--------------------|--------------------|---------------------------------|
| 2H-Q2M135 | 0.55 | 14 | 26 |
| H-Q2M135 | 1.1 | 20 | 18 |
| HB-Q2M135 | 1.4 | 22 | 16 |
| HBs-Q2M135 | 1.4 | 22 | 16 |
| HBss-Q2M135 | 1.5 | 23 | 15 |
| B-Q2M135 | 1.7 | 24 | 14 |
| Bs-Q2M135 | 1.9 | 25 | 13 |
| Bss-Q2M135 | 2.2 | 27 | 12 |
| 2H-Q3M135 | 0.64 | 15 | 23 |
| H-Q3M135 | 1.4 | 22 | 16 |
| HB-Q3M135 | 1.6 | 23 | 14 |
| B-Q3M135 | 1.8 | 24 | 13 |
| 2H-Q2M12 | 0.41 | 12 | 30 |
| H-Q2M12 | 0.74 | 16 | 21 |
| HB-Q2M12 | 0.89 | 18 | 20 |
| B-Q2M12 | 1.1 | 20 | 18 |
| HB-Q3M12 | 1.2 | 21 | 18 |
| B-Q3M12 | 1.4 | 23 | 16 |

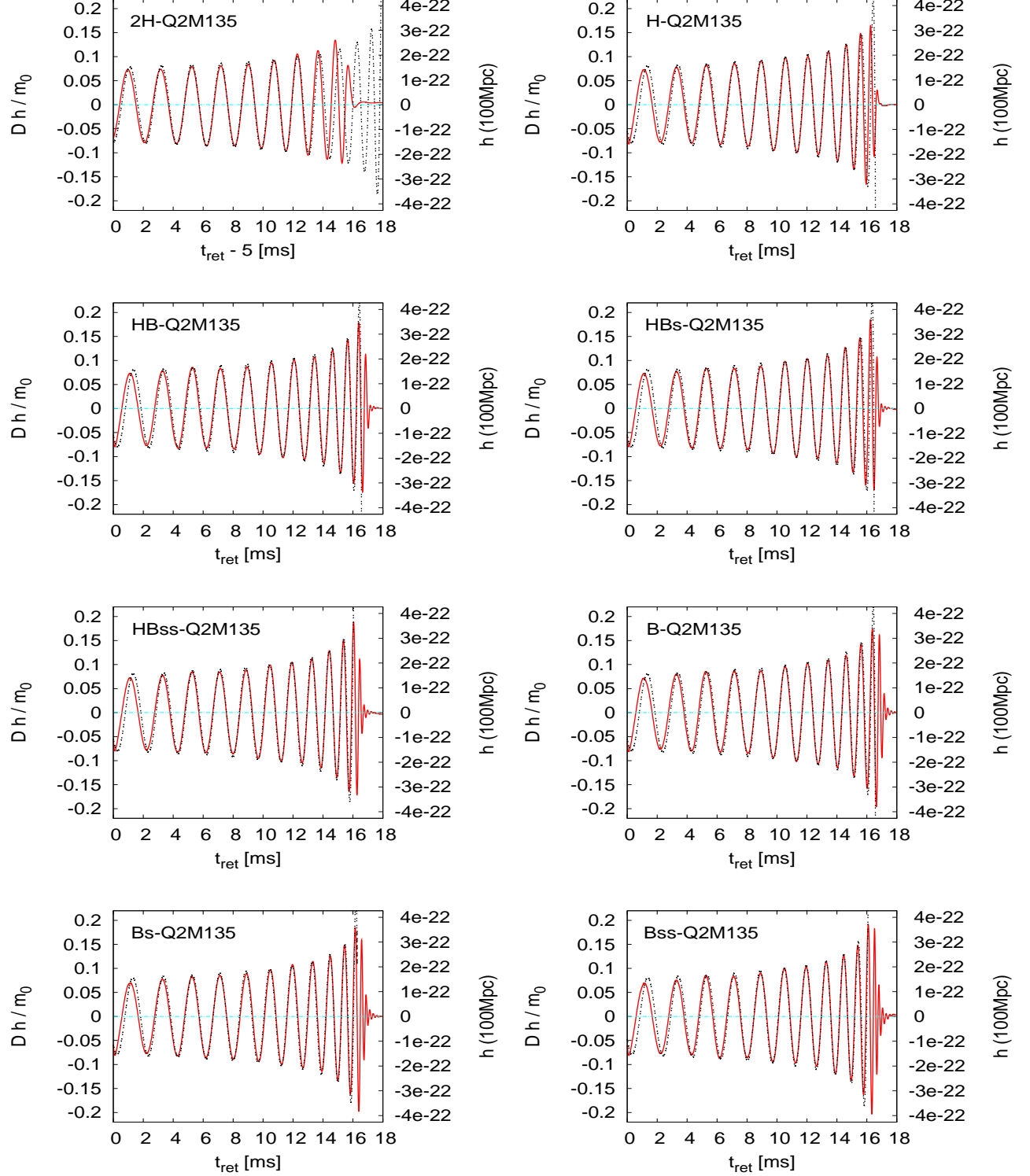


FIG. 6. $(l, m) = (2, 2)$, plus-mode gravitational waveforms for models 2H-Q2M135, H-Q2M135, HB-Q2M135, HBs-Q2M135, HBss-Q2M135, B-Q2M135, Bs-Q2M135, and Bss-Q2M135. All the waveforms are shown for an observer located along the z axis (axis perpendicular to the orbital plane) and plotted as a function of a retarded time. For model 2H-Q2M135, the waveform is plotted as a function of $t_{\text{ret}} - 5$ ms to align it with other waveforms (note that the initial value of Ω only for this model is smaller than those for other models). The left axis denotes the amplitude normalized by the distance from the binary D and the total mass m_0 . The right axis denotes the physical amplitude of gravitational waves observed at a hypothetical distance 100 Mpc. The dotted curves denote the waveform calculated by the Taylor-T4 formula.

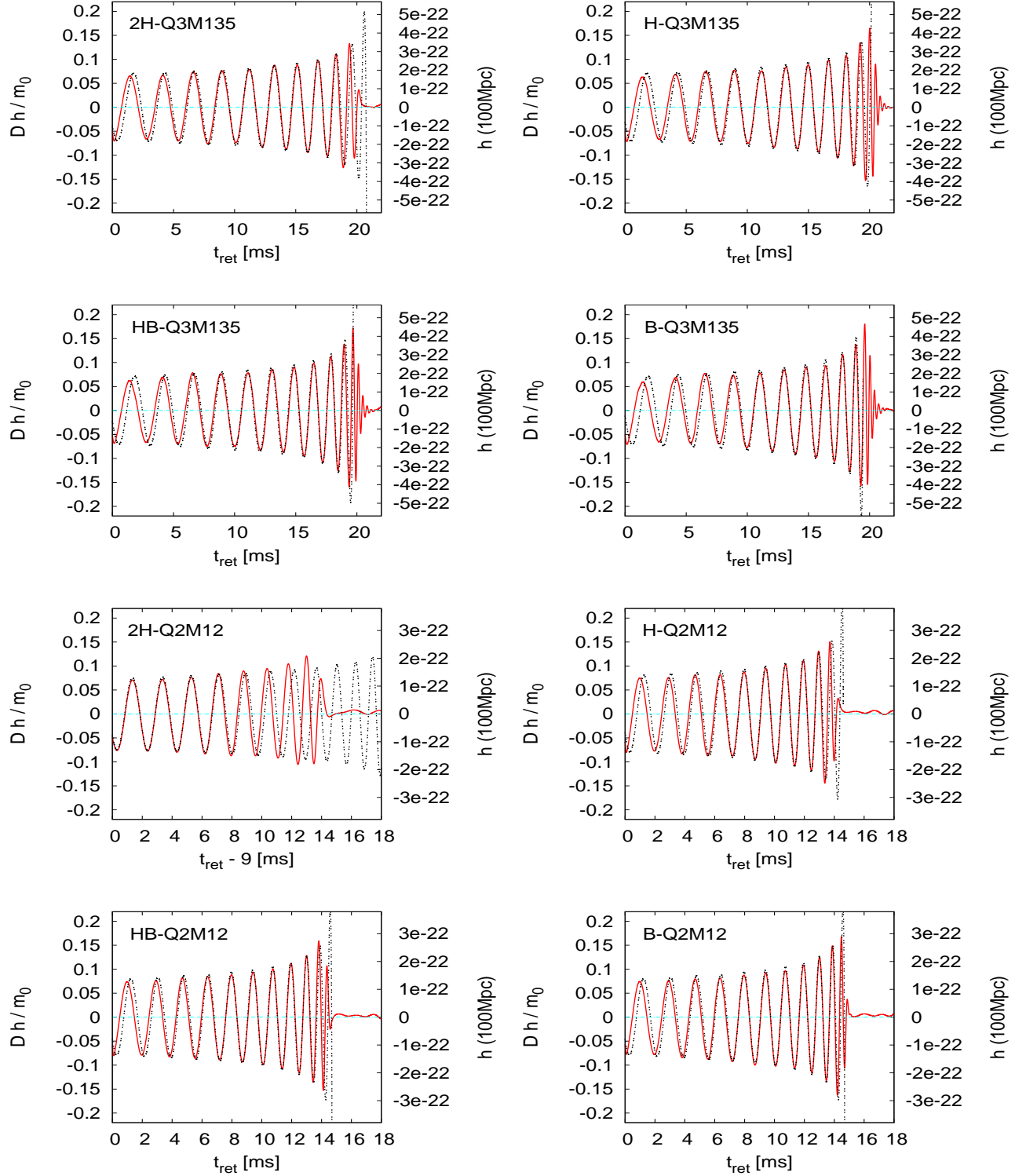


FIG. 7. The same as Fig. 6 but for models 2H-Q3M135, H-Q3M135, HB-Q3M135, B-Q3M135, 2H-Q2M12, H-Q2M12, HB-Q2M12, and B-Q2M12. Again, the waveform for model 2H-Q2M12 is plotted as a function of $t_{\text{ret}} - 9$ ms.

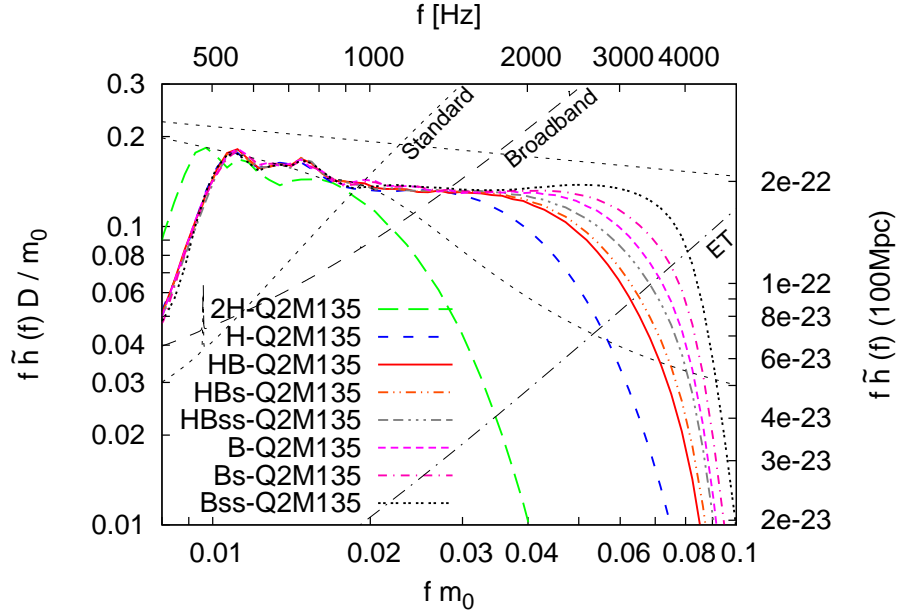


FIG. 8. Spectra of gravitational waves from BH-NS binaries for $Q = 2$ and $M_{\text{NS}} = 1.35M_{\odot}$ with all the EOSs chosen in this paper. The bottom axis denotes the normalized dimensionless frequency $f m_0 (= G f m_0 / c^3)$ and the left axis the normalized amplitude $f \hat{h}(f) D / m_0$. The top axis denotes the physical frequency f in Hz and the right axis the effective amplitude $f \hat{h}(f)$ observed at a distance of 100 Mpc from the binaries. The short-dashed slope line plotted in the upper left region denotes a planned noise curve of the Advanced-LIGO [1] optimized for $1.4M_{\odot}$ NS-NS inspiral detection (“Standard”), the long-dashed slope line denotes a noise curve optimized for the burst detection (“Broadband”), and the dot-dashed slope line plotted in the lower right region denotes a planned noise curve of the Einstein Telescope (“ET”) [54]. The upper transverse dashed line is the spectrum derived by the quadrupole formula and the lower one is the spectrum derived by the Taylor-T4 formula, respectively.

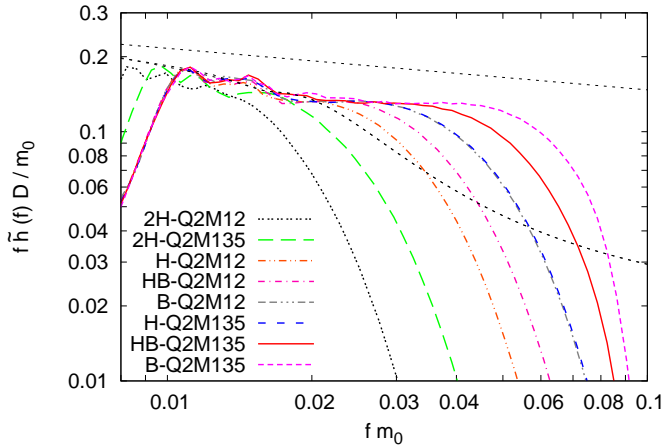


FIG. 9. The same as Fig. 8 but for $Q = 2$ and for $M_{\text{NS}} = 1.35M_{\odot}$ and $1.2M_{\odot}$. Only the normalized amplitude $f \hat{h}(f) D / m_0$ as a function of the dimensionless frequency $f m_0$ is shown.

spurious radiation component does not introduce unphysical oscillations in the gravitational-wave spectrum. The spectrum amplitude for a low-frequency region of $f \approx \Omega(t_{\text{ret}} = 0) / \pi$ changes slightly if we include the spurious radiation component. However, we believe that our

use of the window function is physically reasonable [55]. We always show the spectrum based on gravitational waves observed along the z axis (axis perpendicular to the orbital plane), which is the most optimistic direction for the gravitational-wave detection. (To obtain an averaged amplitude, we only need to multiply a factor of 0.4; e.g., see [52].) Because the Fourier components of any dimensionless quantity have the dimension of time, we define a dimensionless effective amplitude $f \hat{h}(f)$. In the figure, we plot this quantity observed at a hypothetical distance 100 Mpc as a function of f (Hz) or a normalized amplitude $f \hat{h}(f) D / m_0$ as a function of dimensionless frequency $f m_0$.

Figure 8 plots gravitational-wave spectra for $Q = 2$ and $M_{\text{NS}} = 1.35M_{\odot}$ with all the EOSs employed in this paper. For all these models, the total mass is universally $m_0 = 4.05M_{\odot}$, and thus, a nondimensional quantity, $f m_0 (= G f m_0 / c^3)$, is plotted at the bottom and f in units of Hz is plotted at the top. Also, a normalized amplitude, $f \hat{h}(f) D / m_0$, is plotted at the left side and $f \hat{h}(f)$ observed at a distance of 100 Mpc from the binary is at the right side. For comparison, we also plot the spectra derived from the quadrupole formula (e.g., [56]) and the Taylor-T4 formula (dashed curves).

General qualitative features of the gravitational-wave spectrum by BH-NS binaries are summarized as follows. In the early stage of the inspiral phase, during which the

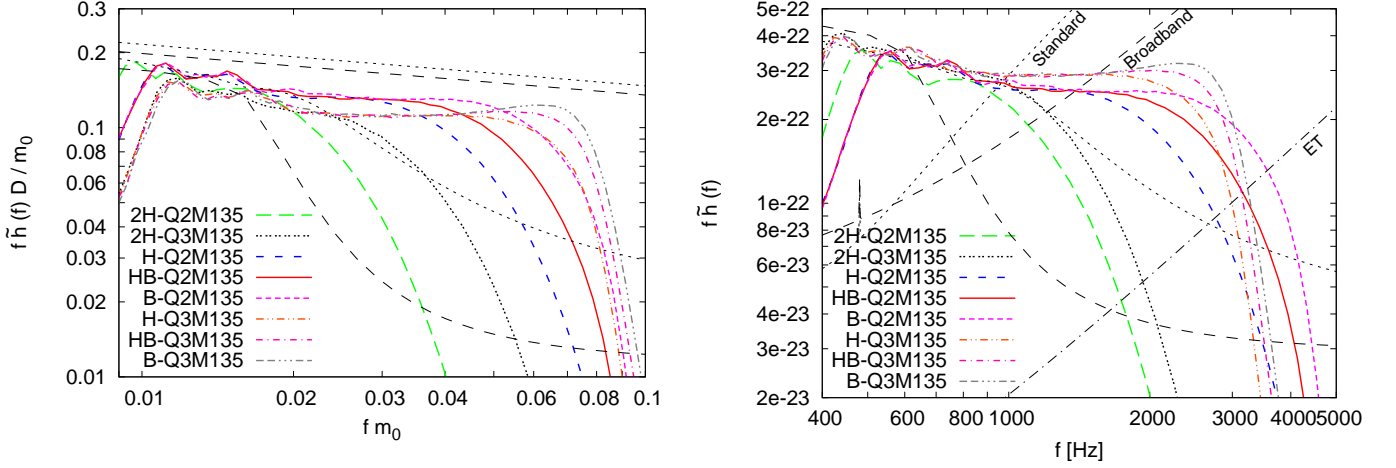


FIG. 10. The same as Fig. 8 but for $M_{\text{NS}} = 1.35M_{\odot}$ and for $Q = 2$ and 3 . The left panel shows the normalized amplitude $f\tilde{h}(f)D/m_0$ as a function of the dimensionless frequency fm_0 . The right panel shows the spectra observed at a distance of 100 Mpc. The spectra derived from the quadrupole formula and the Taylor-T4 formula are plotted by the short-dashed ($Q = 2$) and long-dashed lines ($Q = 3$).

orbital frequency is $\lesssim 1$ kHz and the PN point-particle approximation works well, the gravitational-wave spectrum is approximately reproduced by the Taylor-T4 formula. For this phase, the spectrum amplitude of $f\tilde{h}(f)$ decreases as f^{-n_i} where $n_i = 1/6$ for $f \ll 1$ kHz and the value of n_i increases with f for $f \lesssim 1$ kHz. As the orbital separation decreases, both the nonlinear effect of general relativity and the finite size effect of the NS come into play, and as a result, the PN point-particle approximation breaks down. If the tidal disruption sets in for a relatively large separation (e.g. for 2H EOS), the amplitude of the gravitational-wave spectra damps for a low frequency in the middle of the inspiral phase (before the ISCO is reached). By contrast, if the tidal disruption does not occur or occurs at a close orbit near the ISCO, the spectrum amplitude for a high frequency region ($f \gtrsim 1$ kHz) is larger than that predicted by the Taylor-T4 formula (i.e., the value of n_i decreases). In this case, an inspiral-like motion continues even inside the ISCO for a dynamical time scale and gravitational waves with a high amplitude are emitted. As a result, $f\tilde{h}(f)$ becomes a slowly varying function of f for $1 \text{ kHz} \lesssim f \lesssim f_{\text{cut}}$, where $f_{\text{cut}} \sim 2\text{--}3$ kHz is the so-called cutoff frequency which depends on the binary parameters as well as the EOS of the NSs. (A more strict definition of f_{cut} will be given below.) A steep damping of the spectra for $f \gtrsim f_{\text{cut}}$ is universally observed, and for softer EOSs with a smaller radius of NSs, the frequency of f_{cut} is higher. This cutoff frequency is determined by the frequency of gravitational waves emitted when the NS is tidally disrupted for the stiff EOSs or by the frequency of a quasinormal mode of the formed BH for the soft EOSs. Therefore, the cutoff frequency provides potential information for the EOS through the tidal-disruption event of the NSs, in particular for the stiff EOSs.

Hereafter, we pay special attention to the cutoff fre-

quency determined by the tidal disruption. It is natural to expect that the NS compactness \mathcal{C} primarily determines the cutoff frequency in the combination, $f_{\text{cut}}m_0$, because the orbital angular velocity at the onset of mass shedding, R_{shed} , is written as a function of Q and \mathcal{C} as [14, 15]

$$\Omega m_0 \propto \frac{\mathcal{C}^{3/2}(1+Q)^{3/2}}{\sqrt{Q}}. \quad (46)$$

In fact, we found a qualitative correlation between \mathcal{C} and $f_{\text{cut}}m_0$ in the previous work [24]. To reconfirm this, we first plot gravitational-wave spectra $[f\tilde{h}(f)D/m_0]$ as a function of fm_0 for $Q = 2$ with the different NS mass $M_{\text{NS}} = 1.35M_{\odot}$ and $1.2M_{\odot}$ in Fig. 9. This indeed shows $f_{\text{cut}}m_0$ increases monotonically with \mathcal{C} irrespective of the NS mass for the given mass ratio.

Figure 10 shows the gravitational-wave spectrum for $M_{\text{NS}} = 1.35M_{\odot}$ and for $Q = 2$ and 3 . The left panel plots $f\tilde{h}(f)D/m_0$ as a function of fm_0 and the right panel $f\tilde{h}(f)$ as a function of f for $D = 100$ Mpc. This shows that dependence of $f_{\text{cut}}m_0$ on \mathcal{C} for $Q = 3$ is weaker than for $Q = 2$. The reason for this is that the tidal effect is weaker for $Q = 3$, as discussed in Sec. IV D. (As later shown in Fig. 11, f_{cut} for models H-Q3M135, HB-Q3M135, and B-Q3M135 are not determined by the orbital frequency at tidal disruption but by the quasinormal-mode frequency of the remnant BH, which sets an approximate upper limit on the frequency of gravitational waves emitted in the merger.) Hence, the information of the EOS is not encoded in gravitational waves for $Q = 3$ as strongly as for $Q = 2$. The right panel shows that f_{cut} is between ~ 1 and 3 kHz depending weakly on the value of Q .

To analyze the cutoff frequency quantitatively and to strictly study its dependence on EOSs, we perform a sys-

tematic fitting procedure. As in [24], we fit all the spectra by a function with seven free parameters

$$\tilde{h}_{\text{fit}}(f) = \tilde{h}_{\text{3PN}}(f)e^{-(f/f_{\text{ins}})^{\sigma_{\text{ins}}}} + \frac{Am_0}{Df}e^{-(f/f_{\text{cut}})^{\sigma_{\text{cut}}}}[1 - e^{-(f/f_{\text{ins2}})^{\sigma_{\text{ins2}}}}], \quad (47)$$

where $\tilde{h}_{\text{3PN}}(f)$ is the Fourier spectrum calculated by the Taylor-T4 formula and f_{ins} , f_{ins2} , f_{cut} , σ_{ins} , σ_{ins2} , σ_{cut} , and A are free parameters. The first and second terms of Eq. (47) denote the spectrum models for the inspiral and merger phases, respectively. We determine these free parameters by searching the minimum for a weighted norm defined by

$$\sum_i \left\{ [f_i \tilde{h}(f_i) - f_i \tilde{h}_{\text{fit}}(f_i)] f_i^{1/3} \right\}^2, \quad (48)$$

where i denotes the data point for the spectrum. In the previous work [24], we fix $\sigma_{\text{ins}} = 3.5$ and $\sigma_{\text{ins2}} = 5$ to save the computational costs. Here, these are chosen to be free parameters to reproduce a more consistent spectrum with the original one.

Among these seven free parameters, we focus on f_{cut} because it depends most strongly on the compactness \mathcal{C} and the EOS of the NS. Figure 11 plots $f_{\text{cut}}m_0$, obtained in this fitting procedure, as a function of \mathcal{C} . Also the typical quasinormal-mode frequencies, f_{QNM} , of the remnant BH calculated in Sec. IV D are plotted by the two horizontal lines, which show that the values of $f_{\text{cut}}m_0$ for models H-Q3M135, HB-Q3M135, and B-Q3M135 agree approximately with f_{QNM} and indicates that f_{cut} for these models are irrelevant to the tidal disruption. For $Q = 3$, $f_{\text{cut}}m_0$ depends clearly on the EOS only for $\mathcal{C} \lesssim 0.16$. This agrees with the result with $\Gamma = 2$ polytropic EOS [24]. By contrast, $f_{\text{cut}}m_0$ for $Q = 2$ depends strongly on the NS compactness \mathcal{C} irrespective of M_{NS} not only for the piecewise polytropic EOS but also for $\Gamma = 2$ polytrope [24]. The solid line in Fig. 11 is the linear fitting of $\ln(f_{\text{cut}}m_0)$ as a function of $\ln(\mathcal{C})$ for $Q = 2$ and for the piecewise polytrope with $\Gamma_2 = 3$, and denoted by a well-approximated relation

$$\ln(f_{\text{cut}}m_0) = (3.87 \pm 0.12) \ln \mathcal{C} + (4.03 \pm 0.22). \quad (49)$$

Thus, $f_{\text{cut}}m_0$ is approximately proportional to $\mathcal{C}^{3.9}$ (for $Q = 3$ and $\Gamma_2 = 3$, $f_{\text{cut}}m_0$ also appears to be proportional to \mathcal{C}^4 , although the number of data points is small and thus this is not conclusive). This is a noteworthy point because the power of \mathcal{C} is much larger than 1.5, which is expected from the relation for the mass-shedding limit, Eq. (46). Qualitatively, this increase in the power is natural because the duration of a NS for the survival against tidal disruption after the onset of mass shedding is in general longer for a more compact NS due to a stronger central condensation of the mass. Equation (49) implies that the ratio $f_{\text{cut}}/f_{\text{shed}} (> 1)$, where f_{shed} is the frequency of gravitational waves at the onset of mass shedding, is larger for the larger values of \mathcal{C} . This is the

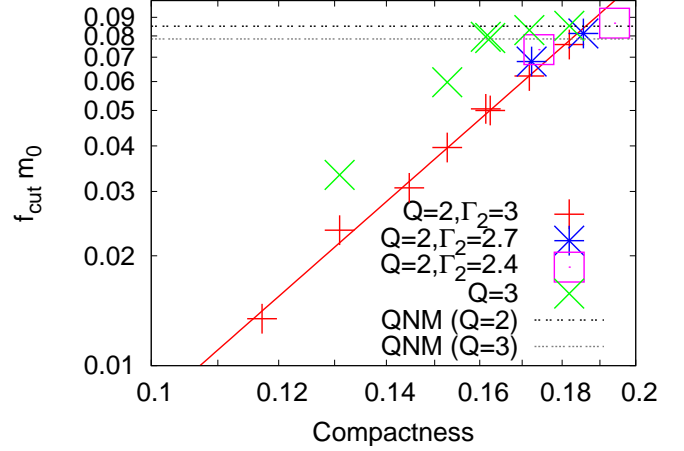


FIG. 11. $f_{\text{cut}}m_0$ as a function of \mathcal{C} in logarithmic scales. The solid line is obtained by a linear fitting of the data for $Q = 2$ and $\Gamma_2 = 3$. The short-dashed and long-dashed lines show approximate frequencies of quasinormal mode of the remnant BH for $Q = 2$ and $Q = 3$, respectively.

preferable feature, for an observer of gravitational waves from BH-NS binaries who tries to constrain the EOS of the NSs, because the dependence of $f_{\text{cut}}m_0$ on the EOS is enhanced.

Comparison of the values of $f_{\text{cut}}m_0$ for models HB-Q2M135 ($\Gamma_2 = 3.0$ and $\mathcal{C} = 0.1718$), HBs-Q2M135 ($\Gamma_2 = 2.7$ and $\mathcal{C} = 0.1723$), and HBss-Q2M135 ($\Gamma_2 = 2.4$ and $\mathcal{C} = 0.1741$), for which the value of \mathcal{C} is approximately identical, shows that $f_{\text{cut}}m_0$ depends also on the adiabatic index of EOS in the central region, Γ_2 . The reason for this is that the NSs with smaller values of Γ_2 (but with the same value of \mathcal{C}) have more centrally condensed density profile as can be seen from the value of ρ_{max} in Table II, and hence, are less subject to tidal disruption ($f_{\text{cut}}m_0$ becomes larger). Quantitatively, the value of $f_{\text{cut}}m_0$ increases by $\sim 20\%$, when the value of Γ_2 is varied from 3 to 2.4. This result suggests that it may be possible to constrain not only the compactness of a NS but also its density profile and detailed function of $P(\rho)$ for the EOS, if gravitational waves emitted during the merger of low-mass BH-NS binaries are detected.

D. Properties of the disk

If a NS is tidally disrupted before it is swallowed by the companion BH, a disk may be formed around the BH. Figure 12 plots the time evolution of the rest mass of the material located outside the apparent horizon $M_{r>r_{\text{AH}}}$ defined by Eq. (41). This shows that most of the material is swallowed by the BH soon after the onset of the merger (or tidal disruption) within ~ 1 ms, but 1%–10% of total rest mass survives around the BH to be a disk, if the tidal disruption occurs (see Table V which lists the numerical results of $M_{r>r_{\text{AH}}}$ at the end of the simulations for all

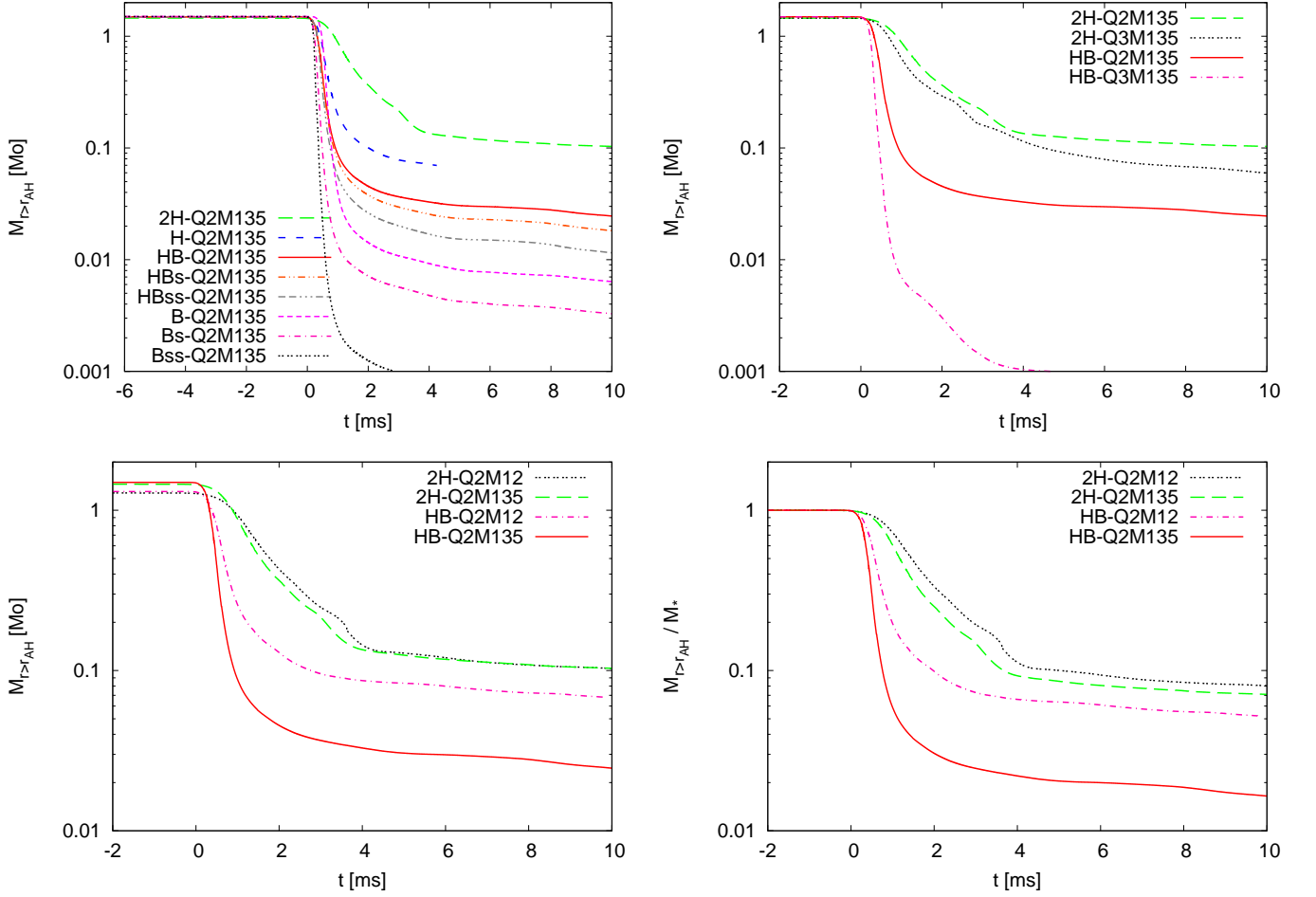


FIG. 12. Evolution of the rest mass of the material located outside the apparent horizon, $M_{r>r_{\text{AH}}}$, with an appropriate time shift; in these plots, the time at the onset of the merger is taken as the time origin. The top-left panel shows the results for models with $Q = 2$ and $M_{\text{NS}} = 1.35M_{\odot}$ for all the EOSs employed in this paper (we note that the simulation for model H-Q2M135 unfortunately terminated in the middle of the accretion process due to the electrical outage at our institute). The top-right panel shows the results for selected models with $M_{\text{NS}} = 1.35M_{\odot}$ but with different values of Q . The bottom-left panel shows the results for selected models with $Q = 2$ but with the different NS mass M_{NS} . The bottom-right panel is the same as the bottom-left panel except for the normalization of the mass, with respect to the initial rest mass M_* .

the models).

To clarify that the disk will survive for a time duration longer than the dynamical time scale of the system, we estimate an accretion time scale. Figure 12 shows that for $t - t_{\text{merger}} \gtrsim 5$ ms, $M_{r>r_{\text{AH}}}$ for each model behaves approximately as $C \exp(-t/t_d)$ where C is a constant and t_d is the accretion time scale which we determine by a least-square fitting of $M_{r>r_{\text{AH}}}(t)$ at $t - t_{\text{merger}} \approx 10$ ms. The fourth column of Table V lists the numerical results. It is found that the accretion time scale is always longer than the dynamical time scale of the remnant disk ~ 10 ms, and hence, we conclude that the BH-NS merger always forms a long-lived accretion disk, if the disk is formed [57].

Figure 13 plots the values of $M_{r>r_{\text{AH}}}$ estimated at $t - t_{\text{merger}} \approx 10$ ms as a function of the NS compactness \mathcal{C} and clarifies the dependence of the disk mass on

the EOS. The disk mass for model Bss-Q2M135 is estimated at the end of the simulations, 4.83 ms, because it already became very small at that time and we stopped the simulation. (We also note that the result for model H-Q2M135 is not included in Fig. 13, because the simulation for this model unfortunately terminated just after the disk formation due to the electrical outage at our institute.) This figure summarizes the key features as follows: (i) for a given mass ratio and for a given adiabatic index of the core, Γ_2 , the disk mass decreases monotonically with the increase of \mathcal{C} for $M_{r>r_{\text{AH}}} \lesssim 0.1M_{\odot}$; (ii) for a given mass ratio and for a given NS compactness, the disk mass increases slightly with the increase of Γ_2 ; and (iii) the disk mass is highly sensitive to the mass ratio of the binary, Q , for a given mass and EOS of the NS. In the following, we observe these features from Fig. 12 in detail.

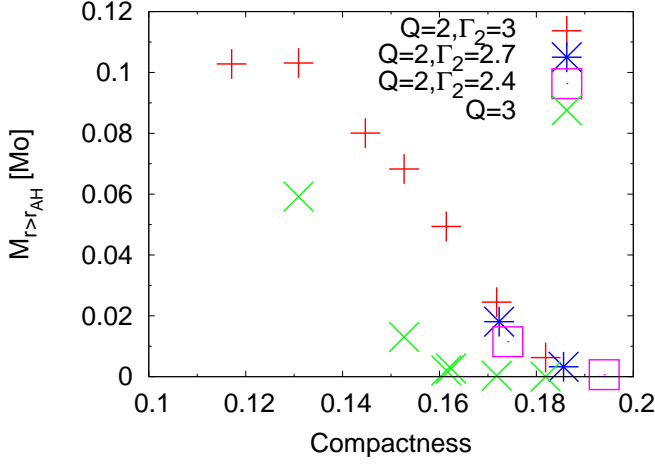


FIG. 13. Disk mass $M_{r>r_{\text{AH}}}$ at $t - t_{\text{merger}} \approx 10$ ms as a function of the NS compactness \mathcal{C} . Note that the disk mass for model Bss-Q2M135 is estimated at the end of the simulations, 4.83 ms, because it became already very small at that time and we stopped the simulation.

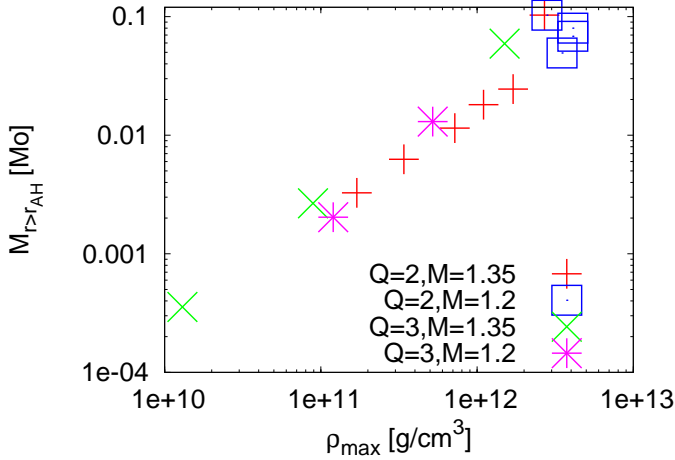


FIG. 14. Relation between disk mass $M_{r>r_{\text{AH}}}$ and the maximum density, ρ_{max} , estimated at $t - t_{\text{merger}} \approx 10$ ms. The maximum density oscillates with time even in the quasistationary phase, and we here plot a value averaged in one oscillation period.

The top left panel of Fig. 12 plots the disk-mass evolution for binaries with $Q = 2$, $M_{\text{NS}} = 1.35M_{\odot}$ and for all the EOSs employed in this paper. For this sample, $\mathcal{C} \propto R_{\text{NS}}^{-1}$ since M_{NS} is identical, and we find that the disk mass increases monotonically with \mathcal{C}^{-1} (see Table I for \mathcal{C} of each model); the disk mass is larger for a model for which the tidal disruption occurs at a more distant orbit (i.e., for smaller value of f_{cut} , cf. Fig. 11). This is quite reasonable because the earlier onset of tidal disruption helps more materials to remain outside the ISCO of the BH.

Comparison of the results for models HB-Q2M135 ($\Gamma_2 = 3.0$ and $\mathcal{C} = 0.1718$), HBs-Q2M135 ($\Gamma_2 = 2.7$

and $\mathcal{C} = 0.1723$), and HBss-Q2M135 ($\Gamma_2 = 2.4$ and $\mathcal{C} = 0.1741$) indicates that the disk mass depends not only on the compactness of the NS but also on the adiabatic index of the core, Γ_2 ; a higher value of Γ_2 is preferable for forming a massive disk. This dependence on Γ_2 is consistent with the result reported in [58]; the NS with a larger value of the adiabatic index is more subject to tidal disruption (tidal disruption occurs for more distant orbital separation). The physical interpretation for this result is that the degree of central mass concentration for NSs of larger values of the adiabatic index is weaker, helping earlier tidal disruption (in other words, we may say that the tidal Love number or deformability is larger for the larger value of Γ_2).

The top right panel of Fig. 12 plots the disk-mass evolution for the NS with the same mass ($M_{\text{NS}} = 1.35M_{\odot}$) but with different mass ratio $Q = 2$ and $Q = 3$ and with HB and 2H EOSs. This, together with Fig. 13, shows that the disk mass depends strongly on the mass ratio, in particular for the soft EOS. The reason for this is simply that the NS is less subject to tidal disruption for a larger BH mass (i.e., for weaker tidal force near the ISCO). The present result suggests that the disk mass is much smaller than $0.01M_{\odot}$ for BH-NS binaries with the typical NS mass of $M_{\text{NS}} = 1.2\text{--}1.35M_{\odot}$ and $\mathcal{C} \gtrsim 0.16$, if the BH is nonspinning and $M_{\text{BH}} \gtrsim 4M_{\odot}$. Only for the case $\mathcal{C} \lesssim 0.16$, the disk mass may be larger than $0.01M_{\odot}$ even with a high-mass BH companion. This conclusion is in agreement with the previous studies [22–24].

The two bottom panels of Fig. 12 compare the disk-mass evolution for models 2H-Q2M12 and 2H-Q2M135 and for models HB-Q2M12 and HB-Q2M135. In the left panel we plot the disk mass in units of M_{\odot} while the bottom right panel plots the disk mass in units of M_{*} . We note that the NS radius depends weakly on the mass for $1.2M_{\odot} \leq M_{\text{NS}} \leq 1.35M_{\odot}$ for both EOSs, and also the mass ratio Q is identical for these models. Nevertheless, the disk mass depends strongly on the NS mass except for models with stiff 2H EOS as seen in Table V; it decreases with the increase of M_{NS} . Thus, not the NS radius R_{NS} but \mathcal{C} is the key parameter for determining the disk mass.

Before closing this section, we summarize several key properties of the remnant disk. Figure 14 plots the relation between $M_{r>r_{\text{AH}}}$ and the maximal rest-mass density ρ_{max} of the remnant disk estimated at $t - t_{\text{merger}} \approx 10$ ms. This clearly shows a strong correlation between two quantities. The value of $M_{r>r_{\text{AH}}}$ increases approximately linearly with ρ_{max} for $M_{r>r_{\text{AH}}} \lesssim 0.1M_{\odot}$, and for $M_{r>r_{\text{AH}}} \geq 0.01M_{\odot}$, ρ_{max} is larger than 4×10^{11} g/cm³. Because the density is high and the temperature should be also high enough (~ 10 MeV if viscous effects or magnetohydrodynamic effects are taken into account [59–61]), neutrinos will be copiously produced in such a disk in reality. Because of the high density and temperature, the cross section to the nucleon will be large enough ($\sim 10^{-41}$ cm²) to trap neutrinos inside the disk of nucleon number density $n_n = \rho/m_n \gtrsim 10^{35}$ cm⁻³ where m_n is nucleon mass 1.66×10^{-24} g [62–64]. Therefore,

a neutrino-dominated accretion disk will be always produced, if BH-NS binaries result in a system composed of the BH and surrounding disk of mass larger than $0.01M_\odot$.

E. Properties of the remnant BH

Table V shows several quantities associated with the remnant BH such as the mass and spin, in addition to the disk mass. Unlike the disk mass, the mass and spin of the remnant BH depend weakly on the EOS of the NS. For given values of Q and M_{NS} , the BH mass tends to be slightly smaller for stiffer EOS, primarily because the fraction of the NS mass swallowed by the BH is smaller (the disk mass is larger). The spin does not show such a clear dependence. The reason is that the spin angular momentum of the remnant BH is affected by two competing processes; one is the orbital angular momentum dissipation due to gravitational radiation reaction and the other is the distribution of the angular momentum to the disk surrounding the BH. The former dissipation effect is important for the case in which the NS is compact and the tidal disruption does not occur as stated in Sec. IV B. By contrast, the latter effect is more important for the case in which the NS is less compact and the tidal disruption occurs in the relatively early stage of the inspiral phase. Although the relation $\Delta J > J_{r>r_{\text{AH}}}$ (where $J_{r>r_{\text{AH}}}$ denotes the angular momentum of disk) always holds for all the models, we may also have the relation $\Delta E \gtrsim M_{r>r_{\text{AH}}}$. As a result, a nondimensional spin parameter, which may be approximately estimated by

$$\frac{\text{Spin angular momentum}}{(\text{Mass})^2} \approx \frac{(J_0 - \Delta J - J_{r>r_{\text{AH}}})}{(M_0 - \Delta E - M_{r>r_{\text{AH}}})^2}, \quad (50)$$

does not depend simply on the EOS.

The spin of the remnant BH is primarily determined by the mass ratio, Q ; $a = 0.66 \pm 0.03$ for $Q = 2$ and $a = 0.54 \pm 0.02$ for $Q = 3$ (here \pm signs do not imply the error bars but signify differences due to the EOS). Thus, the spin parameter is modified by the EOS only in $\pm 5\%$.

From the typical value of the spin parameter a and mass of the remnant BH $M_{\text{BH,f}}$, we estimate typical quasinormal-mode frequencies f_{QNM} of the remnant BH by the latest fitting formula [65]

$$f_{\text{QNM}} M_{\text{BH,f}} \approx \frac{1}{2\pi} [1.5251 - 1.1568(1 - a)^{0.1292}]. \quad (51)$$

Then, $f_{\text{QNM}} \approx 0.083/M_{\text{BH,f}}$ for $Q = 2$ and $\approx 0.076/M_{\text{BH,f}}$ for $Q = 3$, respectively. Assuming that $C_e/4\pi$ gives an approximate value of $M_{\text{BH,f}}$ as described in Sec. III B, these values are in good agreement with the ringdown part of gravitational waves for models Bss-Q2M135 and B-Q3M135, for which the disk masses are negligibly small, respectively. We note that this estimation is valid only when the quasinormal modes of the BH

are excited, and actually the tidal disruption of the NS often suppresses the quasinormal-mode excitation as can be seen in Figs. 6 and 7, in particular, for the stiff EOS such as 2H.

V. SUMMARY

We performed numerical simulations for the merger of nonspinning BH-NS binaries using an AMR code SACRA with eight piecewise polytropic EOSs. In this work, we employed the EOSs with two free parameters which determine the core EOSs. The crust EOS was fixed whereas the core EOS was varied for a wide range, to investigate the dependence of gravitational waveforms, merger process, and merger remnant on the core EOS. We focused, in particular, on the case in which the NS is tidally disrupted by the companion BH, choosing relatively low values of mass ratio as $Q = 2$ and 3 as well as low masses for the NS as $M_{\text{NS}} = 1.2$ and $1.35M_\odot$. By preparing the initial condition with a distant orbit and a small eccentricity, we always tracked $\gtrsim 5$ quasicircular orbits in the inspiral phase and studied the merger phase with a realistic setting. We also evolved the merger remnant (BH-disk system) until they settled to a quasistationary state.

A wide variety of simulations were systematically performed to investigate the dependence of the tidal-disruption process and resulting gravitational waveforms on the EOS. For the case in which the tidal disruption occurs before the orbit reaches the ISCO, the gravitational-wave amplitude decreases quickly at its onset and the emission of ringdown gravitational waves associated with the quasinormal mode of the remnant BH is suppressed. Only in the BH-NS binaries with low values of mass ratio (for the nonspinning BH), the tidal effects play an important role, and hence, the remarkable dependence of the gravitational waveforms on the EOS is found only for such cases: With stiffer EOSs, the radius of the NS becomes larger and the tidal effect is more relevant than with softer EOSs. For given masses of the BH and NS, the tidal disruption occurs in a lower frequency with stiffer EOSs than with softer EOSs, and consequently, the emission of gravitational waves terminates at a lower frequency in the inspiral phase. The corresponding Fourier spectrum of gravitational waves is characterized by a cutoff frequency, f_{cut} , above which the spectrum amplitude exponentially damps. From the analysis of the gravitational-wave spectra, we find that the cutoff frequency f_{cut} depends strongly on the mass ratio and the compactness \mathcal{C} of the NS. For a given small mass ratio such as $Q = 2$, the value of f_{cut} increases monotonically and steeply with \mathcal{C} , depending weakly on the adiabatic index, Γ_2 , of the core EOS. We derive the relation between \mathcal{C} and f_{cut} for $Q = 2$ and $\Gamma_2 = 3$ as $f_{\text{cut}} \propto \mathcal{C}^{3.9}$, in which the power index of \mathcal{C} is significantly larger than 1.5 which is expected from the analysis of the mass-shedding limit. This implies that the dependence of f_{cut} on \mathcal{C} is

TABLE V. Several key quantities for the merger remnants. All the quantities are estimated when we stopped the simulation at $t = t_{\text{end}}$. t_{merger} denotes the time of the merger and the time duration for following the disk evolution, $t_{\text{end}} - t_{\text{merger}}$, is shown in the second column. $M_{r>r_{\text{AH}}}$ is the rest mass of the disk surrounding the BH; because the accretion is still ongoing at the end of simulations due to the hydrodynamic angular momentum transport process, the values listed give only an approximate mass of the long-lived accretion disk (especially for model H-Q2M135; see Sec. IV D), which survives for a time scale longer than the dynamical time scale ~ 10 ms. t_d is the approximate accretion time scale estimated around ~ 10 ms after the merger, which we show only for the case $M_{r>r_{\text{AH}}} \gtrsim 0.001M_{\odot}$. C_e and C_p are the circumferential radii of the apparent horizon along the equatorial plane and meridional plane, respectively, and $C_e/4\pi$ is the approximate mass of the remnant BH. M_{irr} is the irreducible mass of the remnant BH. a is the nondimensional spin parameter of the remnant BH estimated from C_p/C_e .

| Model | $t_{\text{end}} - t_{\text{merger}}$ (ms) | $M_{r>r_{\text{AH}}}[M_{\odot}]$ | t_d (ms) | $C_e/4\pi M_0$ | M_{irr}/M_0 | C_p/C_e | a |
|-------------|---|----------------------------------|------------|----------------|----------------------|-----------|------|
| 2H-Q2M135 | 12.6 | 0.097 | 30 | 0.947 | 0.891 | 0.913 | 0.64 |
| H-Q2M135 | 4.22 | 0.070 | ... | 0.968 | 0.905 | 0.905 | 0.66 |
| HB-Q2M135 | 11.9 | 0.022 | 18 | 0.978 | 0.912 | 0.902 | 0.67 |
| HBs-Q2M135 | 13.7 | 0.015 | 15 | 0.980 | 0.914 | 0.902 | 0.67 |
| HBss-Q2M135 | 13.5 | 0.0093 | 12 | 0.981 | 0.916 | 0.903 | 0.67 |
| B-Q2M135 | 20.0 | 0.0045 | 20 | 0.980 | 0.917 | 0.905 | 0.66 |
| Bs-Q2M135 | 12.5 | 0.0029 | 19 | 0.979 | 0.917 | 0.906 | 0.66 |
| Bss-Q2M135 | 4.83 | 6×10^{-4} | ... | 0.977 | 0.917 | 0.910 | 0.65 |
| 2H-Q3M135 | 20.4 | 0.044 | 19 | 0.961 | 0.925 | 0.944 | 0.52 |
| H-Q3M135 | 21.4 | 0.0015 | 11 | 0.984 | 0.942 | 0.937 | 0.55 |
| HB-Q3M135 | 16.5 | 2×10^{-4} | ... | 0.983 | 0.942 | 0.937 | 0.55 |
| B-Q3M135 | 15.1 | $< 10^{-5}$ | ... | 0.982 | 0.941 | 0.939 | 0.55 |
| 2H-Q2M12 | 12.6 | 0.097 | 31 | 0.939 | 0.886 | 0.918 | 0.62 |
| H-Q2M12 | 11.9 | 0.077 | 30 | 0.959 | 0.899 | 0.907 | 0.66 |
| HB-Q2M12 | 9.72 | 0.068 | 30 | 0.964 | 0.902 | 0.906 | 0.66 |
| B-Q2M12 | 15.4 | 0.043 | 24 | 0.972 | 0.908 | 0.903 | 0.67 |
| HB-Q3M12 | 12.2 | 0.011 | 15 | 0.979 | 0.937 | 0.937 | 0.55 |
| B-Q3M12 | 10.6 | 0.0019 | 17 | 0.982 | 0.940 | 0.936 | 0.56 |

stronger than that for f_{shed} , and indicates that the observation of f_{cut} will play a role for constraining the value of \mathcal{C} . Varying the core EOS also modifies the value of f_{cut} , because the central density profile of the NS depends on the stiffness of the core EOS and susceptibility to the tidal force of its companion BH is modified. For the variation from $\Gamma_2 = 3$ to 2.4, the value of f_{cut} is modified by $\sim 20\%$. This suggests that the details of the core EOS for $\rho \gtrsim 10^{15}$ g/cm³ may play an important role for determining the gravitational waveform from the BH-NS binaries composed of high-mass NSs.

We also determined the mass of the disk surrounding the remnant BH. The disk mass depends strongly on the EOS, because the EOS determines the location at which the tidal disruption occurs through the compactness \mathcal{C} of the NS. The disk mass is correlated strongly with the NS compactness \mathcal{C} , and for $Q = 2$, it can be $\gtrsim 0.01M_{\odot}$ for a wide range of the EOSs and the NS masses M_{NS} . However, the disk mass is tiny for $Q = 3$, unless the EOS is extremely stiff like 2H EOS or the NS mass is low. For the BH-NS binaries consisting of a nonspinning BH, the disk mass can be $\gtrsim 0.01M_{\odot}$ for $Q = 3$, only for the case $\mathcal{C} \lesssim 0.16$.

Using the quantities calculated on the apparent horizon, we estimated the dimensionless spin parameter of the remnant BH. We find that this spin parameter de-

pends only weakly on the EOS for given masses of the BH and NS, unlike the disk mass. The BH spin depends primarily on the mass ratio Q and becomes smaller for a binary with a larger value of Q : $a \approx 0.66 \pm 0.03$ for $Q = 2$ and $\approx 0.54 \pm 0.02$ for $Q = 3$.

Finally we list the issues for the future. The two-piece EOS employed in this paper is not accurate enough to describe high-mass NSs for which the inner core is composed of a high-density matter with $\rho \gtrsim 10^{15}$ g/cm³. For the study of a BH-NS binary composed of a high-mass NS with small values of Q (i.e., for a binary in which the tidal interaction plays a role), it is necessary to adopt piecewise polytrope EOSs with three or four free parameters. It is also necessary to take into account the BH spin for a systematic survey of the BH-NS binary merger process, because the orbital frequency at the ISCO depends strongly on the BH spin as well as the mass of the BH; e.g., for the ISCO around Kerr BHs, the orbital angular frequency increases by a factor of $6^{3/2}$ if the spin is changed from zero to unity. This difference in the ISCO will be crucial for determining the criteria for the onset of tidal disruption, the mass of the remnant disk, and gravitational waveforms. Currently we are working on this subject and will report the numerical results in the next paper.

TABLE VI. Several numerical results for models HB-Q2M135 and H-Q3M135 with different grid resolutions, $N = 50, 42$, and 36. All the quantities are defined in the body text. In this table, we compare the disk mass at $t - t_{\text{merger}} \approx 10$ ms.

| N | $f_{\text{cut}} m_0$ | $M_{r>r_{\text{AH}}}[M_{\odot}](10\text{ms})$ | a | $\Delta E/M_0(\%)$ | $\Delta J/J_0(\%)$ |
|-----------|----------------------|---|------|--------------------|--------------------|
| HB-Q2M135 | | | | | |
| 50 | 0.0613 | 0.025 | 0.67 | 1.36 | 21.8 |
| 42 | 0.0621 | 0.022 | 0.67 | 1.34 | 21.4 |
| 36 | 0.0644 | 0.022 | 0.68 | 1.35 | 21.4 |
| H-Q3M135 | | | | | |
| 50 | 0.0790 | 0.0027 | 0.55 | 1.39 | 21.8 |
| 42 | 0.0794 | 0.0021 | 0.56 | 1.36 | 21.3 |
| 36 | 0.0788 | 0.0022 | 0.56 | 1.33 | 20.7 |

ACKNOWLEDGMENTS

We thank J.L. Friedman for the suggestion of parameter sets of the piecewise polytrope employed in this paper, for careful reading of this paper, and for helpful comments. Numerical computation of quasiequilibrium states is performed using the free library LORENE [30]. We thank members in the Meudon Relativity Group for developing LORENE. This work was supported by Grant-in-Aid for Scientific Research (21340051), by a Grant-in-Aid for Scientific Research on Innovative Area (20105004) of Japanese MEXT, by a Grant-in-Aid of JSPS, and by a Grant-in-Aid for the Global COE Program “The Next Generation of Physics, Spun from Universality and Emergence” of Japanese MEXT.

APPENDIX: CONVERGENCE

In this Appendix, we demonstrate that the convergence is approximately achieved for the numerical results shown in Sec. IV. We here compare numerical results obtained with different grid resolutions for models HB-Q2M135 and H-Q3M135. Table VI lists several numerical results. This shows that the numerical results depend only weakly on the grid resolutions, and thus, we conclude that the convergence is approximately achieved in our simulation. Most importantly, Fig. 15 shows that the gravitational-wave spectra approximately converge and $f_{\text{cut}} m_0$ shown in Table VI does not vary by $\gtrsim 5\%$. Figure 16 plots $f_{\text{cut}} m_0$ for model HB-Q2M135 as a function of the inverse of a squared grid resolution $1/N^2$. This figure shows that the value of $f_{\text{cut}} m_0$ converges at better than second order, and thus the values of $f_{\text{cut}} m_0$ for $N = 50$ are obtained in $\lesssim 3\%$ error. For model H-Q3M135, the value of $f_{\text{cut}} m_0$ does not converge systematically and fluctuates with the amplitude of $\sim 0.5\%$. This fluctuation may be ascribed to the variance associated with the fitting procedure using Eq. (47), which involves a number of free parameters. We estimate roughly the variance of $f_{\text{cut}} m_0$ at $\sim 0.5\%$ within 95% accuracy of the fitting with respect to the

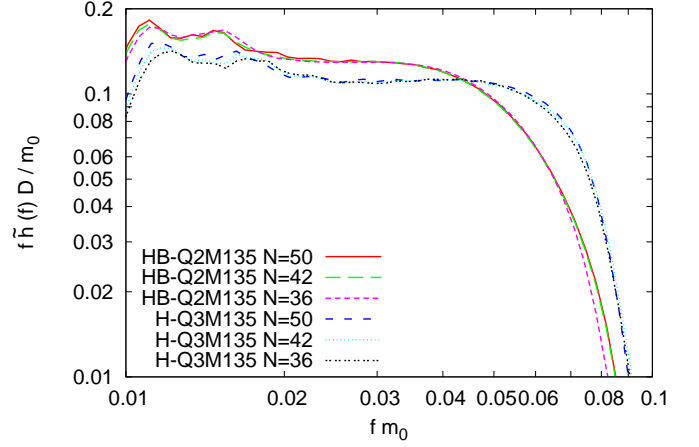


FIG. 15. Comparison of gravitational-wave spectra for models HB-Q2M135 and H-Q3M135 with different grid resolutions.

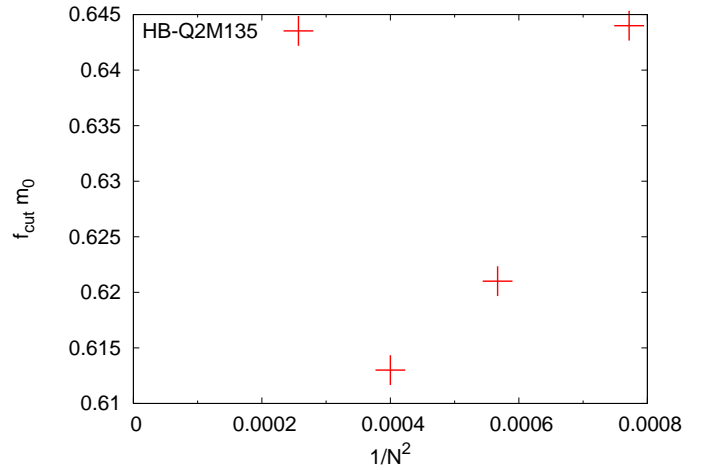


FIG. 16. $f_{\text{cut}} m_0$ as a function of the inverse of a squared grid resolution $1/N^2$ for model HB-Q2M135.

norm defined by Eq. (48) for model H-Q3M135. We note that the merger time t_{merger} depends on the grid resolution; it is systematically larger for better grid resolutions. However, the spectrum near $f = f_{\text{cut}}$ depends weakly on the grid resolution. ΔE and ΔJ also approximately converge. The errors are $\lesssim 0.1\%$ for ΔE and $\lesssim 1\%$ for ΔJ , respectively.

Among many quantities, the disk mass is most sensitive to the numerical dissipation because the spurious dissipation of the angular momentum in the disk enhances the accretion of the materials surrounding BH and results in a lower disk mass. Hence, the values of disk mass described in the body text should be regarded as the lower limit of the actual mass of the remnant disk.

We plot the time evolution of the disk mass for different grid resolutions in Fig. 17. Roughly speaking, the numerical results for the disk mass increase with improving the grid resolution, although systematic convergence

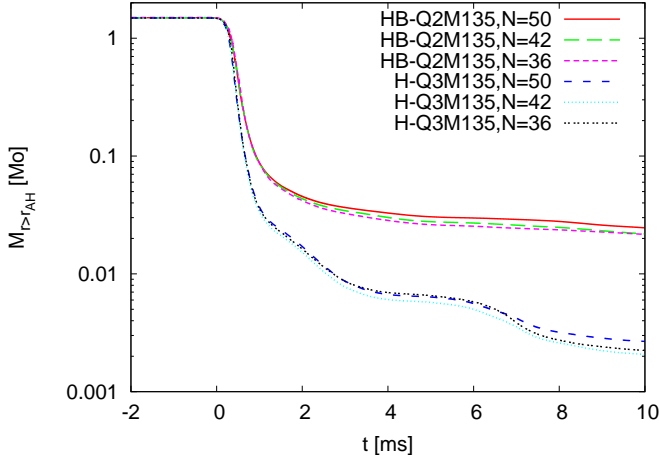


FIG. 17. Comparison of the disk-mass evolution for models HB-Q2M135 and H-Q3M135 with different grid resolutions.

property is not seen. The reason for this unsystematic behavior is likely that the motion of the disk material is affected slightly by the atmosphere (in particular for low-mass disks of relatively low densities), and thus, convergence property should not be expected. Assuming most conservatively that the convergence is achieved only at first order for the results of $N = 42$ and 50 , the error of the results for $N = 50$ may be a factor of 2 for the low disk mass case $M_{r>r_{AH}} \lesssim 0.01 M_{\odot}$. However, we expect that systematic quantitative relations between the disk mass and the compactness of the NS, and between the disk mass and the maximum density shown in Figs. 13 and 14 are not drastically changed.

VI. ERRATUM

(The original version of this article was submitted on Aug 9, 2010. This erratum is added on Aug 5, 2011.)

In previous sections, we performed numerical simulations for the merger of a nonspinning black hole (BH) and a neutron star (NS), and explored gravitational waves emitted and the final outcome formed after the merger. We recently noticed that we systematically *underestimated* disk masses in previous sections. The reason is that we evolved hydrodynamic variables and estimated disk masses only in domains of the size $\sim 200^3 \text{ km}^3$, although Einstein's field equation was solved in domains of the size $\sim 800^3 \text{ km}^3$. A small domain size for hydrodynamics is insufficient for the estimation of the disk mass, because, if tidal disruption occurs at a distant orbit, especially for the case in which the NS radius is large ($\sim 15 \text{ km}$), tidal disrupted material extends far away from the central region. For this reason, we performed again the same simulations as in previous sections, enlarging the computational domain of hydrodynamics. To estimate disk mass more accurately, in addition, we enlarged the size of the computational domain to the size

TABLE VII. Setup of the grid structure for the computation with our AMR algorithm. $\Delta x = h_7 = L/(2^7 N)$ is the grid spacing at the finest-resolution domain with L being the location of the outer boundaries for each axis. $R_{\text{diam}}/\Delta x$ denotes the grid number assigned inside the semimajor diameter of the NS. λ_0 is the gravitational wavelength of the initial configuration.

| Model | $\Delta x/M_0$ | $R_{\text{diam}}/\Delta x$ | L/λ_0 |
|-------------|----------------|----------------------------|---------------|
| 2H-Q2M135 | 0.0471 | 90.8 | 2.377 |
| H-Q2M135 | 0.0377 | 86.2 | 2.130 |
| HB-Q2M135 | 0.0347 | 87.0 | 1.963 |
| HBs-Q2M135 | 0.0353 | 85.2 | 1.996 |
| HBss-Q2M135 | 0.0353 | 84.0 | 1.996 |
| B-Q2M135 | 0.0330 | 85.1 | 1.863 |
| Bs-Q2M135 | 0.0324 | 84.4 | 1.830 |
| Bss-Q2M135 | 0.0270 | 95.4 | 1.650 |
| 2H-Q3M135 | 0.0353 | 89.0 | 1.996 |
| H-Q3M135 | 0.0282 | 84.7 | 1.711 |
| HB-Q3M135 | 0.0269 | 82.7 | 1.631 |
| B-Q3M135 | 0.0247 | 83.8 | 1.497 |
| 2H-Q2M12 | 0.0565 | 86.9 | 2.510 |
| H-Q2M12 | 0.0453 | 83.1 | 2.563 |
| HB-Q2M12 | 0.0420 | 83.6 | 2.377 |
| B-Q2M12 | 0.0392 | 83.4 | 2.218 |
| HB-Q3M12 | 0.0306 | 84.6 | 1.713 |
| B-Q3M12 | 0.0278 | 86.9 | 1.572 |

$1500^3\text{--}2000^3 \text{ km}^3$. This is done by increasing a coarse domain by one more level in the adaptive mesh refinement algorithm (AMR). Specifically, the number of coarser domains is increased from three to four. Table VII (new version of Table III) summarizes the parameters of the new grid structure. In these simulations, the total rest mass of the atmosphere is always less than $10^{-4} M_{\odot}$. Results for gravitational waves do not change within the level of numerical accuracy in our simulations.

Table VIII (corrected version of Table V) lists corrected values for quantities associated with the merger remnants. We estimated all the values at the end of the simulations in previous sections. In this section, we present the values evaluated at $\approx 10 \text{ ms}$ after the merger to perform more systematic comparisons. Quantities associated with the remnant BH do not change appreciably. Taking into account the change in the time at which the disk mass is estimated, the mass of the remnant disk becomes larger by a factor of $\sim 2\text{--}3$ for $Q = 2$, and by a factor of ~ 5 for $Q = 3$. Figure 18 (corrected version of Fig. 12) plots the time evolution of $M_{r>r_{AH}}$. Although qualitative behavior is not altered, $M_{r>r_{AH}}$ is systematically larger for the new computations. In particular, the sudden decrease of $M_{r>r_{AH}}$ at $\sim 3\text{--}5 \text{ ms}$ after the merger seen in Fig. 12 now disappears. Approximate accretion time scale t_d becomes longer by a factor of $\lesssim 2$ for many cases. Figure 19 (corrected version of Fig. 13)

plots the values of $M_{r>r_{\text{AH}}}$ at ≈ 10 ms after the merger as a function of \mathcal{C} . Although we again see the systematic increase of $M_{r>r_{\text{AH}}}$, the conclusion that the disk mass is much smaller than $0.01M_{\odot}$ for BH-NS binaries with the typical NS mass of $M_{\text{NS}} = 1.2\text{--}1.35M_{\odot}$ and $\mathcal{C} \gtrsim 0.16$ does not change. Figure 20 (corrected version of Fig. 14) plots the relation between $M_{r>r_{\text{AH}}}$ and the maximum rest mass density ρ_{max} of the remnant disk. Approximately

speaking, the relations between them are not changed qualitatively and quantitatively.

Table IX (corrected version of Table VI) lists several numerical results for the merger remnants, and Fig. 21 (corrected version of Fig. 17) plots the time evolution of $M_{r>r_{\text{AH}}}$ for different grid resolutions. The convergence of the remnant disk mass becomes slightly better than that in previous sections.

-
- [1] B. P. Abbott et al., Rep. Prog. Phys. **72**, 076901 (2009).
 - [2] F. Acernese et al., Class. Quantum Grav. **25**, 114045 (2008).
 - [3] The LIGO Scientific Collaboration and The Virgo Collaboration, Nature **460**, 990 (2009).
 - [4] V. Kalogera, K. Belczynski, C. Kim, R. O’Shaughnessy, and B. Willems, Phys. Rep. **442**, 75 (2007).
 - [5] K. Belczynski, R. E. Taam, V. Kalogera, F. A. Rasio, and T. Bulik, Astrophys. J. **662**, 504 (2007).
 - [6] E. Nakar, Phys. Rep. **442**, 166 (2007).
 - [7] W. H. Lee and E. Ramirez-Ruiz, New J. Phys **9**, 17 (2007).
 - [8] R. D. Blandford and R. D. Znajek, Mon. Not. Roy. Astron. Soc. **179**, 433 (1977).
 - [9] L. Lindblom, Astrophys. J. **398**, 569 (1992).
 - [10] M. Vallisneri, Phys. Rev. Lett. **84**, 3519 (2000).
 - [11] J. S. Read, C. Markakis, M. Shibata, K. Uryū, J. D. E. Creighton, and J. L. Friedman, Phys. Rev. D **79**, 124033 (2009).
 - [12] V. Ferrari, L. Gualtieri, and F. Pannarale, Phys. Rev. D **81**, 064026 (2010).
 - [13] P. Grandclément, Phys. Rev. D **74**, 124002 (2006); **75**, 129903(E) (2007).
 - [14] K. Taniguchi, T. W. Baumgarte, J. A. Faber, and S. L. Shapiro, Phys. Rev. D **75**, 084005 (2007).
 - [15] K. Taniguchi, T. W. Baumgarte, J. A. Faber, and S. L. Shapiro, Phys. Rev. D **77**, 044003 (2008).
 - [16] F. Foucart, L. E. Kidder, H. P. Pfeiffer, and S. A. Teukolsky, Phys. Rev. D **77**, 124051 (2008).
 - [17] K. Kyutoku, M. Shibata, and K. Taniguchi, Phys. Rev. D **79**, 124018 (2009).
 - [18] M. Shibata and K. Uryū, Phys. Rev. D **74**, 121503(R) (2006).
 - [19] M. Shibata and K. Uryū, Class. Quant. Grav. **24**, S125 (2007).
 - [20] M. Shibata and K. Taniguchi, Phys. Rev. D **77**, 084015 (2008).
 - [21] Z. B. Etienne, J. A. Faber, Y. T. Liu, S. L. Shapiro, K. Taniguchi, and T. W. Baumgarte, Phys. Rev. D **77**, 084002 (2008).
 - [22] M. D. Duez, F. Foucart, L. E. Kidder, H. P. Pfeiffer, M. A. Scheel, and S. A. Teukolsky, Phys. Rev. D **78**, 104015 (2008).
 - [23] Z. B. Etienne, Y. T. Liu, S. L. Shapiro, and T. W. Baumgarte, Phys. Rev. D **79**, 044024 (2009).
 - [24] M. Shibata, K. Kyutoku, T. Yamamoto, and K. Taniguchi, Phys. Rev. D **79**, 044030 (2009).
 - [25] M. D. Duez, F. Foucart, L. E. Kidder, C. D. Ott, and S. A. Teukolsky, Class. Quant. Grav. **27**, 114106 (2010).
 - [26] J. S. Read, B. D. Lackey, B. J. Owen, and J. L. Friedman, Phys. Rev. D **79**, 124032 (2009).
 - [27] F. Özel and D. Psaltis, Phys. Rev. D **80**, 103003 (2009).
 - [28] In the original piecewise polytropic EOS, finite-temperature effects are not taken into account. In our numerical simulation, a correction of finite temperature induced by shock heating is taken into account; see Sec. III A.
 - [29] In this paper, the stiffness is simply determined by the magnitude of pressure for the nuclear-density region. We do not determine it by the adiabatic index.
 - [30] LORENE website, <http://www.lorene.obspm.fr/>.
 - [31] G. B. Cook, Living Rev. Relativity **3**, 5 (2000).
 - [32] L. Bildsten and C. Cutler, Astrophys. J. **400**, 175 (1992).
 - [33] C. S. Kochanek, Astrophys. J. **398**, 234 (1992).
 - [34] R. Beig, Phys. Lett. A **69**, 153 (1978).
 - [35] A. Ashtekar and A. Magnon-Ashtekar, J. Math. Phys. **20**, 793 (1979).
 - [36] S. Brandt and B. Brügmann, Phys. Rev. Lett. **78**, 3606 (1997).
 - [37] L. Blanchet, Phys. Rev. D **65**, 124009 (2002).
 - [38] J. M. Lattimer and M. Prakash, Science **304**, 536 (2004).
 - [39] I. H. Stairs, Science **304**, 547 (2004).
 - [40] J. M. Lattimer and M. Prakash, Astrophys. J. **550**, 426 (2001).
 - [41] T. Yamamoto, M. Shibata, and K. Taniguchi, Phys. Rev. D **78**, 064054 (2008).
 - [42] M. Shibata and T. Nakamura, Phys. Rev. D **52**, 5428 (1995).
 - [43] T. W. Baumgarte and S. L. Shapiro, Phys. Rev. D **59**, 024007 (1998).
 - [44] M. Campanelli, C. O. Lousto, P. Marronetti, and Y. Zlochower, Phys. Rev. Lett. **96**, 111101 (2006).
 - [45] J. G. Baker, J. Centrella, D.-I. Choi, M. Koppitz, and J. van Meter, Phys. Rev. Lett. **96**, 111102 (2006).
 - [46] B. Brügmann, J. A. González, M. Hannam, S. Husa, U. Sperhake, and W. Tichy, Phys. Rev. D **77**, 024027 (2008).
 - [47] A. Kurganov and E. Tadmor, J. Comput. Phys. **160**, 241 (2000).
 - [48] M. Shibata, K. Taniguchi, and K. Uryū, Phys. Rev. D **71**, 084021 (2005).
 - [49] C. Reisswig and D. Pollney, arXiv:1006.1632.
 - [50] In the previous work, we subtract quadratic functions by the least-square fitting also from Ψ_4 itself and $\int \Psi_4 dt$. We have found that we do not have to perform this procedure.
 - [51] M. Boyle, D. A. Brown, L. E. Kidder, A. H. Mroué, H. P. Pfeiffer, M. A. Scheel, G. B. Cook, and S. A. Teukolsky, Phys. Rev. D **76**, 124038 (2007).
 - [52] A. Buonanno, G. B. Cook, and F. Pretorius, Phys. Rev. D **75**, 124018 (2007).
 - [53] L. E. Kidder, Phys. Rev. D **77**, 044016 (2008).

TABLE VIII. Several key quantities for the merger remnants. All the quantities are estimated at $t - t_{\text{merger}} \approx 10$ ms, where t_{merger} denotes the time of the merger. $M_{r>r_{\text{AH}}}$ is the rest mass of the disk surrounding the BH; because the accretion is still ongoing at the end of simulations due to the hydrodynamic angular momentum transport process, the values listed give only an approximate mass of the long-lived accretion disk, which survives for a time scale longer than the dynamical time scale ~ 10 ms. t_d is the approximate accretion time scale estimated around ≈ 10 ms after the merger, which we show only for the case $M_{r>r_{\text{AH}}} \gtrsim 0.001M_\odot$. C_e and C_p are the circumferential radii of the apparent horizon along the equatorial plane and meridional plane, respectively, and $C_e/4\pi$ is the approximate mass of the remnant BH. M_{irr} is the irreducible mass of the remnant BH. a is the nondimensional spin parameter of the remnant BH estimated from C_p/C_e .

| Model | $M_{r>r_{\text{AH}}}[M_\odot]$ | t_d (ms) | $C_e/4\pi M_0$ | M_{irr}/M_0 | C_p/C_e | a |
|-------------|--------------------------------|------------|----------------|----------------------|-----------|------|
| 2H-Q2M135 | 0.20 | 57 | 0.942 | 0.886 | 0.913 | 0.64 |
| H-Q2M135 | 0.076 | 32 | 0.969 | 0.905 | 0.903 | 0.67 |
| HB-Q2M135 | 0.032 | 24 | 0.978 | 0.912 | 0.902 | 0.67 |
| HBs-Q2M135 | 0.024 | 22 | 0.980 | 0.914 | 0.902 | 0.67 |
| HBss-Q2M135 | 0.014 | 21 | 0.980 | 0.915 | 0.902 | 0.67 |
| B-Q2M135 | 0.0085 | 18 | 0.980 | 0.916 | 0.904 | 0.67 |
| Bs-Q2M135 | 0.0053 | 23 | 0.980 | 0.917 | 0.906 | 0.66 |
| Bss-Q2M135 | 7×10^{-4} | ... | 0.977 | 0.917 | 0.910 | 0.65 |
| 2H-Q3M135 | 0.19 | 26 | 0.958 | 0.923 | 0.945 | 0.52 |
| H-Q3M135 | 0.013 | 26 | 0.982 | 0.940 | 0.936 | 0.56 |
| HB-Q3M135 | 0.0022 | 25 | 0.983 | 0.941 | 0.936 | 0.56 |
| B-Q3M135 | 2×10^{-4} | ... | 0.982 | 0.941 | 0.938 | 0.55 |
| 2H-Q2M12 | 0.21 | 66 | 0.937 | 0.885 | 0.918 | 0.62 |
| H-Q2M12 | 0.12 | 28 | 0.958 | 0.900 | 0.907 | 0.66 |
| HB-Q2M12 | 0.091 | 31 | 0.965 | 0.902 | 0.905 | 0.66 |
| B-Q2M12 | 0.065 | 27 | 0.970 | 0.906 | 0.903 | 0.67 |
| HB-Q3M12 | 0.044 | 30 | 0.977 | 0.936 | 0.937 | 0.55 |
| B-Q3M12 | 0.011 | 28 | 0.982 | 0.939 | 0.935 | 0.56 |

TABLE IX. The disk masses at $t - t_{\text{merger}} \approx 10$ ms and nondimensional spin parameters of the remnant BHs for models HB-Q2M135 and H-Q3M135 with different grid resolutions, $N = 50, 42$, and 36 .

| N | $M_{r>r_{\text{AH}}}[M_\odot](10\text{ms})$ | a |
|-----------|---|------|
| HB-Q2M135 | | |
| 50 | 0.032 | 0.67 |
| 42 | 0.031 | 0.67 |
| 36 | 0.030 | 0.67 |
| H-Q3M135 | | |
| 50 | 0.013 | 0.56 |
| 42 | 0.013 | 0.56 |
| 36 | 0.013 | 0.56 |

[54] S. Hild, S. Chelkowski, and A. Freise, arXiv:0810.0604.

[55] In the previous work [24], we matched the Taylor-T4 waveform with numerical waveforms in the inspiral phase to compensate lack of numerical waveforms at low frequencies, and then, performed the Fourier transformation. In the present work, we do not perform such a procedure, because that is not necessary to study the depen-

dence of the Fourier spectrum on EOSs near $f \sim f_{\text{cut}}$.

- [56] C. Cutler and É. É. Flanagan, Phys. Rev. D **49**, 2658 (1994).
- [57] Note that in the presence of magnetic fields, angular momentum transport by them works efficiently, and thus, the accretion time scale may be shorter than that presented here in reality.
- [58] M. Ishii, M. Shibata, and Y. Mino, Phys. Rev. D **71**, 044017 (2005).
- [59] S. Setiawan, M. Ruffert, and H.-T. Janka, Astron. Astrophys. **458**, 553 (2006).
- [60] W. H. Lee, E. Ramirez-Ruiz, and D. Page, Astrophys. J. **632**, 421 (2005).
- [61] M. Shibata, Y.-I. Sekiguchi, and R. Takahashi, Prog. Theor. Phys. **118**, 257 (2007).
- [62] R. Narayan, T. Piran, and P. Kumar, Astrophys. J. **557**, 949 (2001).
- [63] T. Di Matteo, R. Perna, and R. Narayan, Astrophys. J. **579**, 706 (2002).
- [64] K. Kohri and S. Mineshige, Astrophys. J. **577**, 311 (2002).
- [65] E. Berti, V. Cardoso, and A. O. Starinets, Class. Quantum Grav. **26**, 163001 (2009).

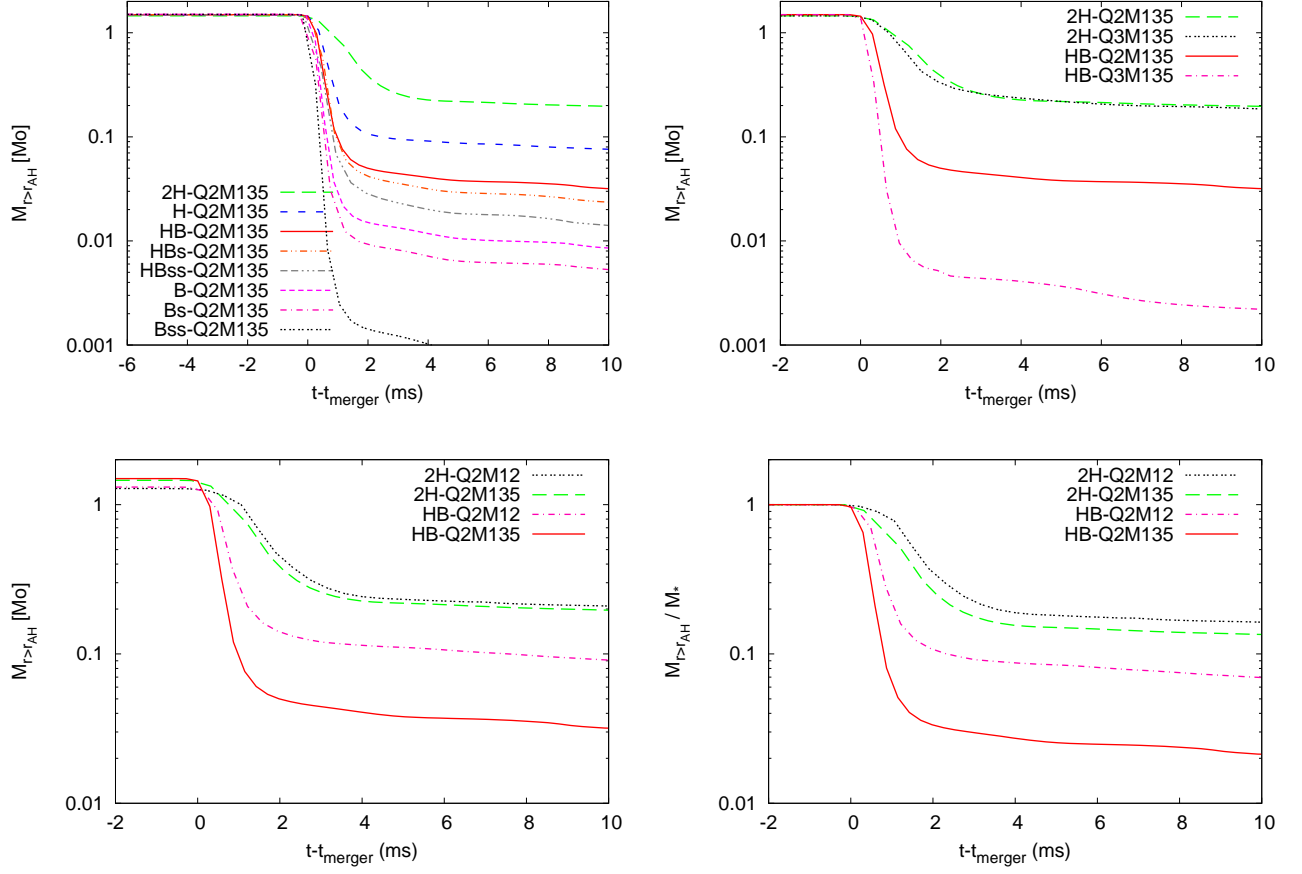


FIG. 18. Evolution of the rest mass of the material located outside the apparent horizon, $M_{r>r_{\text{AH}}}$, with an appropriate time shift; in these plots, the time at the onset of the merger is taken as the time origin. The top-left panel shows the results for models with $Q = 2$ and $M_{\text{NS}} = 1.35 M_{\odot}$ for all the EOSs employed in this paper. The top-right panel shows the results for selected models with $M_{\text{NS}} = 1.35 M_{\odot}$ but with different values of Q . The bottom-right panel is the same as the bottom-left panel except for the normalization of the mass, with respect to the initial rest mass M_* .

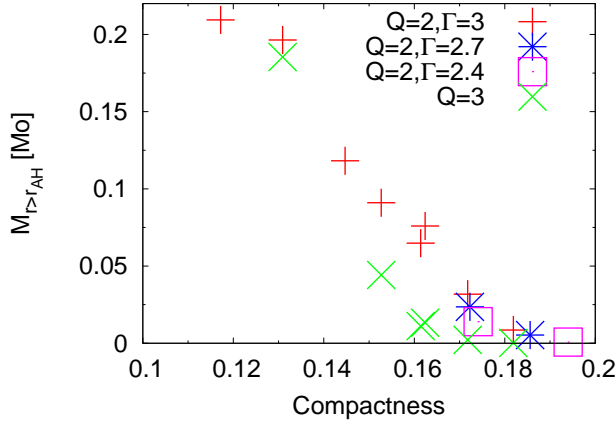


FIG. 19. Disk mass $M_{r>r_{\text{AH}}}$ at $t - t_{\text{merger}} \approx 10$ ms as a function of the NS compactness \mathcal{C} .

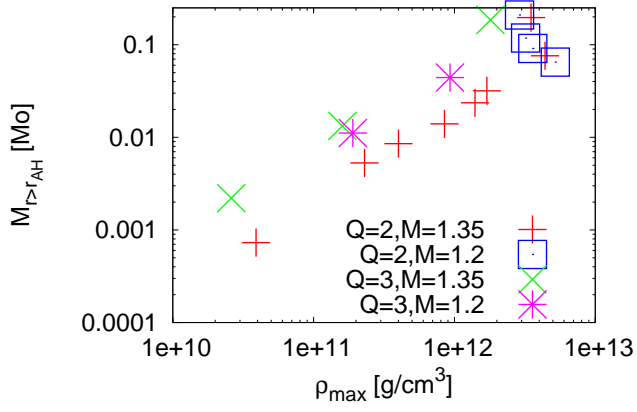


FIG. 20. Relation between disk mass $M_{r>r_{\text{AH}}}$ and the maximum density, ρ_{max} , estimated at $t - t_{\text{merger}} \approx 10$ ms. The maximum density oscillates with time even in the quasistationary phase, and we here plot a value averaged in one oscillation period.

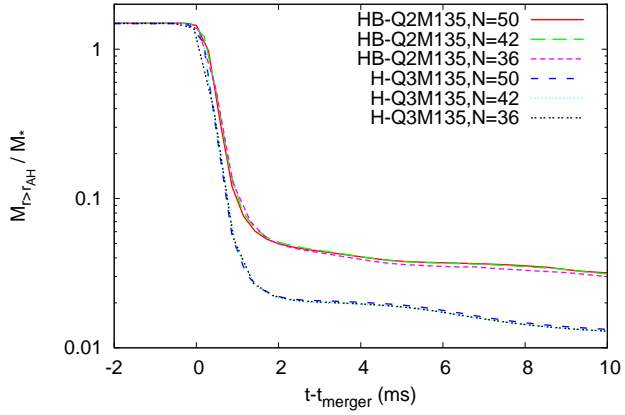


FIG. 21. Comparison of the disk-mass evolution for models HB-Q2M135 and H-Q3M135 with different grid resolutions.